Isogeometric Computational Modeling of Curvilinear Fiber Composites

Kenta Suzuki

A thesis
submitted in partial fulfillment of the
requirements of the degree of

Master of Science in Aeronautics and Astronautics

University of Washington

2019

Reading Committee:

Marco Salviato

Jinkyu Yang

Program Authorized to Offer Degree:
Aeronautics and Astronautics

University of Washington

Abstract

Isogeometric Computational Modeling of Curvilinear Fiber Composites

Kenta Suzuki

Chair of the Supervisory Committee:
Marco Slaviato
Department of Aeronautics and Astronautics

Recently, composite materials are broadly used in a wide range of industries. Composite materials are attractive in designing applications not only because of its outstanding specific mechanical performance but also its ability to tailor the material properties based on design-purpose. Conventional fiber-reinforced composite structures have utilized layup orientation to achieve a desired mechanical performance of a laminate. However, these structures are still limited to straight fibers, which are not necessarily placed in the optimal way to carry the load. Thanks to the advancement in manufacturing technology, emerging technologies such as Automated Fiber Placement (AFP) and Additive Manufacturing (AM) enable complex and large-scale structural designs, especially leveraging on Curvilinear Transverse Isotropy (CTI), in which fibers are deposited along curvilinear paths to optimize the load-carrying capability or other functional properties.

In a geometrical modeling process, it is common to design structures using Computer-Aided Design (CAD) software e.g. AutoCAD, CATIA, SolidWorks, etc., and spline functions are often used to parameterize a geometry. However, in analysis, engineers use Finite Element (FE) software packages e.g. ABAQUS, ANSYS, NASTRAN, etc., in which the geometry does not follow the same definition from the CAD design. Thus, the transition process between CAD file and CAE file takes a huge amount of time for re-meshing, refinements, etc. In addition, FEM approximates a CAD model using polynomial basis/interpolation functions

instead of spline functions. These facts result in inefficient time consumption and obtaining less accurate solution. In order to reduce these burdens, it is necessary to integrate the modeling routine and the analysis to obtain high convergence rate and greater precision of the solution. This integration between geometrical modeling and analysis is referred to as Isogeometric Analysis.

First, the theoretical framework of NURBS-based Isogeometric Analysis will be introduced using variational method under the assumption of linear elasticity and plane stress condition. Then, in order to model CTI composites, new methods of computing stiffness matrix in each integration point on an element will be discussed. Second, the implementation framework will be explained using parallelization and vectorization for the element stiffness evaluation and the assemble routines in MATLAB environment.

Once the IGA solver is built, multiple simulations will be conducted on a semi-circular notched plate of under tensile loading with different types of fiber configuration such as (1) curvilinear fibers following the holomorphic path defined by the conformal mapping, (2) concentric fibers following the semi-circular notch, (3) longitudinal straight fibers, and (4) transverse straight fibers. The IGA implementation will show that it converges much faster than the one from FEM. The mechanical behavior of each plate will be discussed and will be concluded that their mechanical behaviors strongly depend on the fiber orientation.

In addition, an optimization study will also be presented for (1) the minimum stress concentration factor and (2) the minimum Tsai-Wu failure index varying the radius of the semi-circular notch.

The optimal fiber paths will show the significant amount of reduction in terms of stress concentration. On the contrary, the optimal fiber paths for the minimum Tsai-Wu failure index will be converged to the longitudinal straight fiber configuration. This optimization study will also indicate that it is very difficult to conclude the optimal fiber path for the damage progress in terms of Tsai-Wu failure criterion, and thus, progressive failure analysis

(PFA) is needed to identify the best fiber configuration.

TABLE OF CONTENTS

LIST OF FIGURES

LIST OF TABLES

ACKNOWLEDGMENTS

I would first like to thank my advisor Dr. Marco Salviato of the Department of Aeronautics and Astronautics at University of Washington. His passion always made me motivated to work on my research and forwarded me to the right direction with his precise advice and a lot of supports.

I would also like to thank my research mentor Sean E. Phenisee for his supports in my work. His kindness and words gave me self-confidence a lot.

Finally, I must express my gratitude to my parents Mitsuo and Tomomi for providing me with this opportunity to study in the U.S. and watching over me from Japan.

Chapter 1

INTRODUCTION

1.1 Manufacturing of Composite Materials

Recently, composite materials are broadly used in a wide range of industries such as aerospace, automotive, renewable energy and consumer goods. Especially, in aerospace engineering, composite materials are applied to large-scale and complex fundamental structures due to their advantages in lightness and strengths against traditional materials such as steels and metals. Under the advancement of manufacturing technology in the composites industry, novel emerging technologies such as AFP and AM allow to achieve high quality and time-effective automation of composite structures.

Automated Fiber Placement(AFP) process is one of an advanced method of manufacturing composite materials. This method is efficient in manufacturing large composite structures and has proficiency in placing curvilinear fiber paths through an automation. An AFP machine has a computer-controlled robotic arm in order to place composite materials(matrices and fibers) and build a ply at a same time. This manufacturing technique allows to build highly customized composite parts with designated different fiber orientations to achieve an attractive damage tolerance [6, 22].

Additive Manufacturing(AM) is the another technology in manufacturing composite structures, which is also referred to as 3D printing. This process is initially to model a three-dimensional solid using Computer-Aided Design(CAD) or scan it as a CAD file. Then, the CAD model can be sliced into thousands of layers by preparation software. Finally, each layup can be decomposed into multiple materials to form the composite structures. Allowing these selective material usage, composite structures can achieve designated material properties such as stiffness, adhesive properties, etc [11]. It is also possible to place the fibers

following continuous curvilinear fiber paths.

1.2 Curvilinear Transverse Isotropy

These developments of manufacturing technologies have enabled to construct large-scale composite structures with a more sophisticated reinforcement, allowing to design composite structures with true optimal properties. Thanks to these developments, it will be possible to construct composite structures made by Curvilinear Transverse Isotrophy(CTI), whose continuous fibers follows curvilinear paths. CTI materials are currently designed to optimize electric and thermal conductivity, and mechanical performances [28, 26, 10].

1.3 Concept of Isogeometric Analysis

In an engineering industry, it is significantly important to go through simulations prior to experiments in order to cut off the cost. Nowadays, designers generate CAD (Computer-Aided Design) files and these must be translated into the CAE (Computer-Aided Engineering) files to perform a structural analysis. Ted Blacker, Manager of Simulation Sciences, Sandia National Laboratories studied the time consumption in the process of the entire modeling and analysis. According to his study, it approximately takes 80% of an entire time of simulation to create suitable geometry with an appropriate input data and meshes in order to conduct a large-scaled Finite Element Analysis (FEA).

Moreover, geometries of our interests for stress analysis is becoming more complicated. As can be noted in the Figure 1.1, for example, automobiles roughly consists of 3,000 parts, the Boeing 777 consists of over 100,000 parts, and nuclear-powered, ballistic missile-carrying submarines feature more than 1,000,000 parts. Engineering design and analysis are deeply related to each other. Such complex designs are based on a broad range of fields such as structural mechanics, fluid mechanics, acoustics, heat transfer, electromagnetics, etc. However, there is no way to automatically translate from CAD model directly into FE model. As we mentioned above, engineers in an industry have to work 80% of overall time on modeling process and 20% on analysis at Sandia National Laboratory. To resolve this issue,

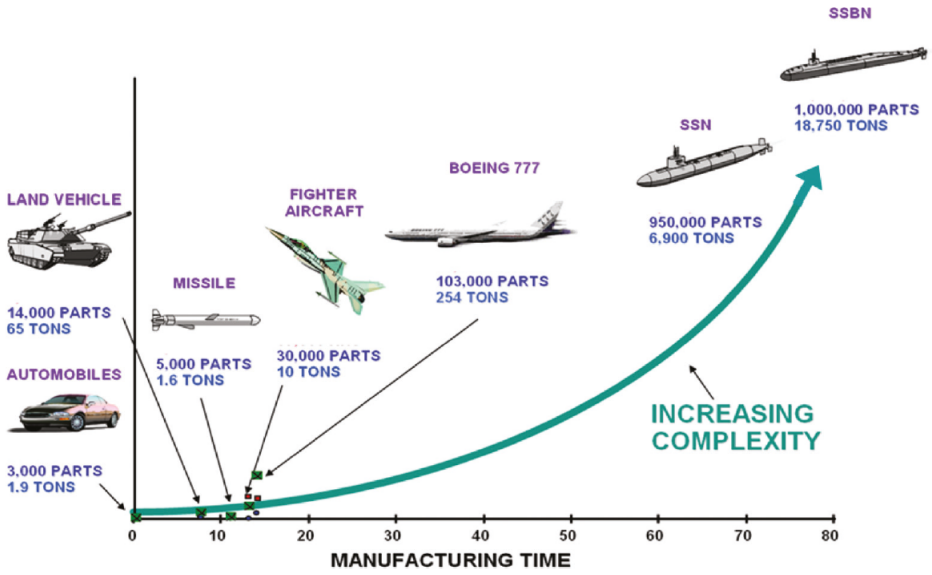

Figure 1.1: Engineering structures are becoming complex and large from [4](Courtesy of General Dynamics / Electric Boat Corporation).

the integration of CAD and FEA should be carried on to reduce the huge amount of time-consumption, which implies that the fundamental changes in the modeling process must be developed [4].

In addition to the integration between CAD and FEA, which reduces time-consumption, current trend in computational engineering is high-performance computing in a sense of accuracy of stress analysis. In FEA, the finite element mesh is an approximation of the CAD model using the basis functions, in contrast to 'exact' geometrical representation in CAD design. This approximated model may cause less accuracy in some cases, for example, shell buckling analysis is very sensitive to the geometry precision (figure 1.2) and sliding contact problem between bodies cannot be expressed without the exact geometries (figure 1.3). To get high rate of convergence and greater precision of analysis, it is very important to create an exact finite element model [4].

To resolve these disadvantages, it is necessary to integrate two entire processes engineering

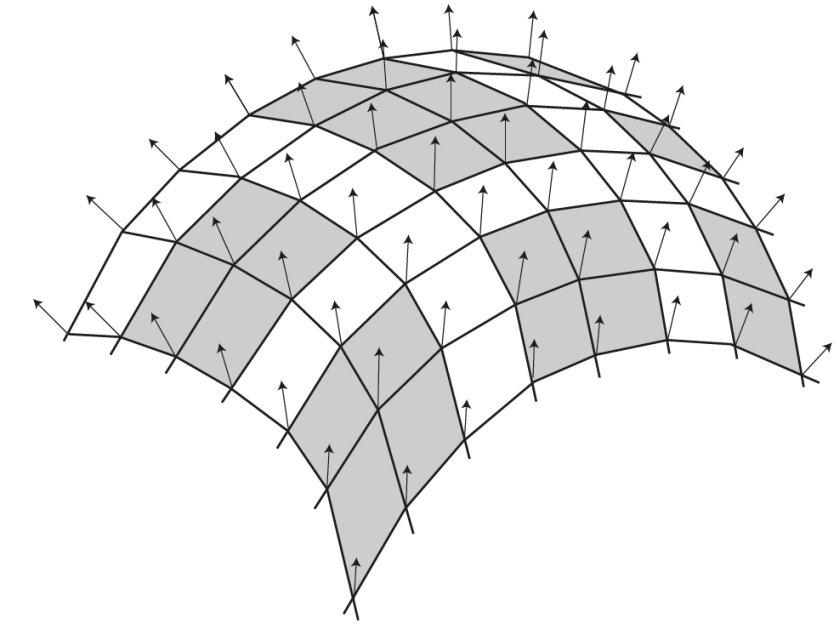

(a)

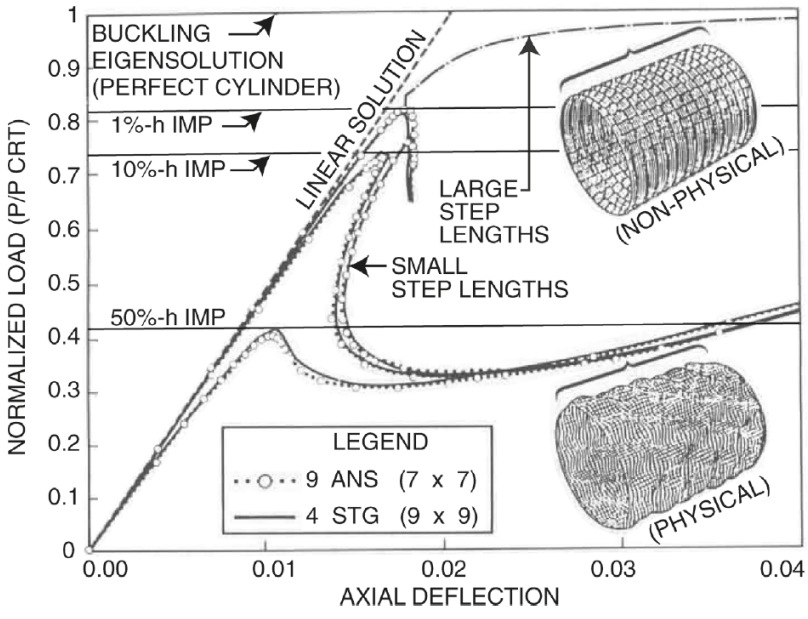

(b)

Figure 1.2: Buckiling shell analysis with imperfect geometries(cited from [4]). (a) classical finite element mesh(adapted from [12]) and (b) the buckling loads significantly depend on the geometry precision(from [29]).

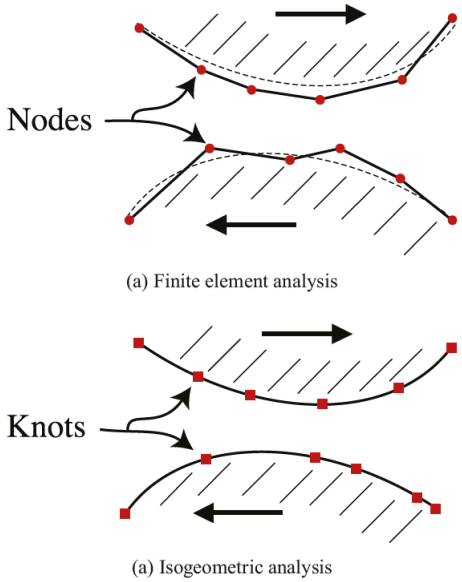

Figure 1.3: Mesh comparison in a sliding contact (cited from [4])between (a) finite element mesh (See [31, 21]) and (b) Isogeometric mesh from [4]

design and analysis. The key is to create an exact geometry directly from CAD file and pass it down to stress analysis based on CAD representations. This concept is refereed to as ***Isogeometric Analysis***, and introduced in Hughes *et al.*, 2005 [17].

1.4 Application of Isogeometric Analysis

Isogeometric Analysis is not only proficient in static problems shown above figure 1.2 and figure 1.3, but also very effective in fluid and fluid-structure interaction using high continuity of the basis functions. For instance, numerical simulation of the Navier-Stokes-Korteweg equations has been implemented by the use of Isogeometric Analysis [14]. It is also utilized to simulate the Taylor-Couette flow for the residual-based variational multi-scale turbulence modeling, and shows good accuracy of the results due to the exact circular geometry expression even though the mesh is very coarse [2]. In addition, Isogeometric Analysis is also utilized in the fluid-structure interaction of an imcompressible fluid on a moving domain

with a nonlinear hyper-elastic solid, e.g. inflation of balloon and flow in a abdominal aorta with aneurysm [3]. The model construction and simulation of aortic valve closure has also been implemented using Isogeometric Analysis, and this shows it is enough for IGA only to refine the mesh with two order of magnitude fewer nodes of FEA [23]. Isogeometric Analysis is also applied on solving partial differential equations such as the Cahn-Hilliard equation which involves fourth-order spatial derivatives [13].

1.5 NURBS-based Isogeometric Analysis

Isogeometric Analysis is an integration between the modeling process and the analysis. It is very common to design some models using CAD package e.g. AutoCAD, CATIA, SolidWorks, etc. These commercial software use spline functions in parameterizing the geometry. In this paper, Non-Uniform Rational B-spline (NURBS) basis function will be used to create an exact geometry, and this function also can be utilized as basis/interpolation functions in a classical FEA.

NURBS has two notations of elements, that are the patch and the knot span. The patch can be defined as one macro-element or subdomain created by knot vectors, which is refereed to as parameter space. Mostly in general, we work on the patch as one model to analyze except the case that we have to deal with the local meshing due to the geometric complexities. Each patch has two different space to express the geometry itself, the one is physical space, and the other is in parent space, which is useful for numerical evaluation. On the other hand, the knot span is the decomposition of the patch and defined by the intervals of knots. The knots are points, lines, and surfaces in one-, two-, and three-dimensional topology, respectively [4].

Figure 1.4 represents the whole image picture of NURBS-based Isogeometric Analysis. The detail of the theoretical framework and implementations are presented in subsequent chapters. The summery of CAD and FEA backgrounds can be found in Hughes *et al.,* 2009 [4].

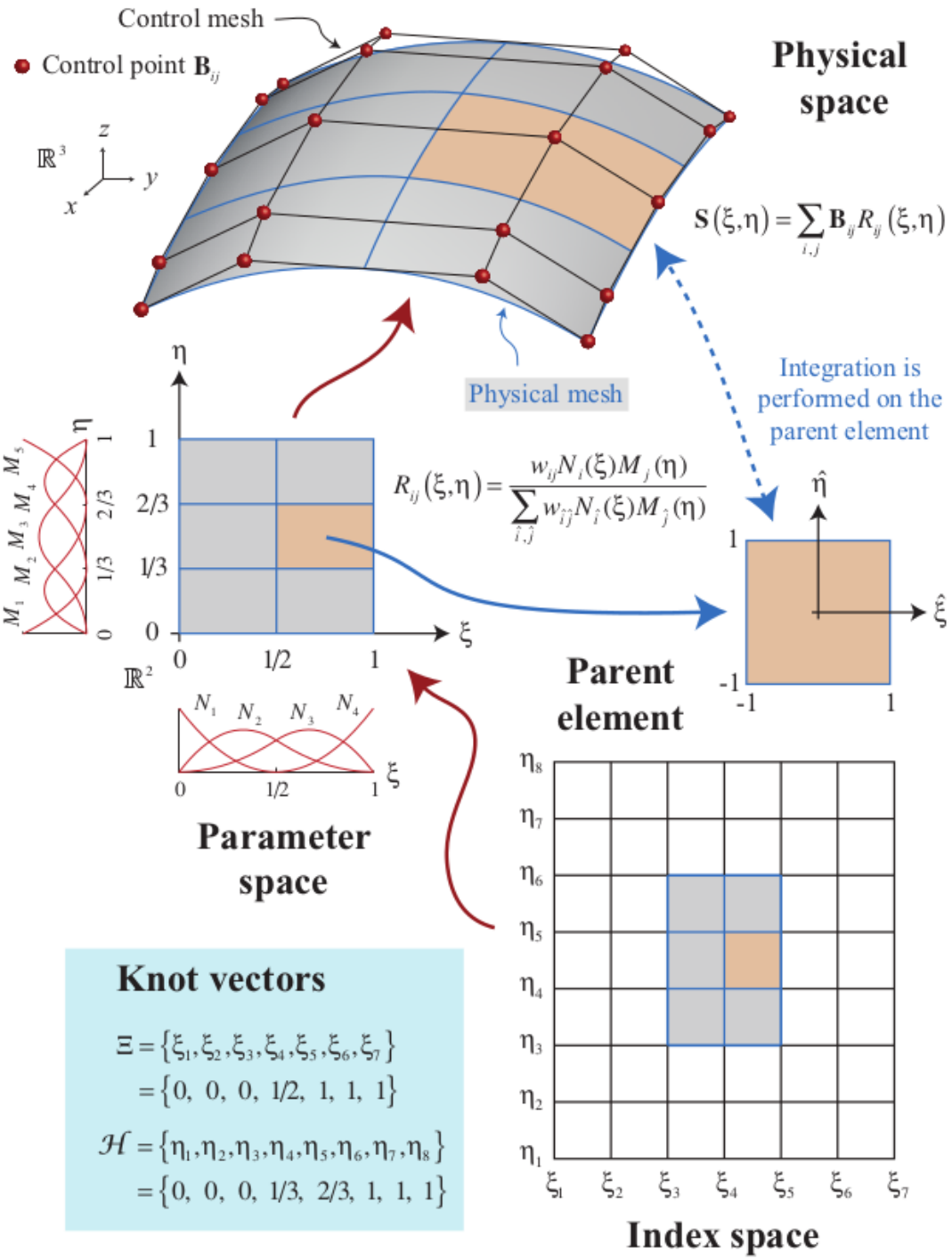

Figure 1.4: Image of NURBS-based IGA Implementation for Two-dimensional one-patch surface model describing three different spaces, parameter, parent, and physical space (cited from [4]).

Chapter 2

THEORETICAL FRAMEWORK OF IGA

2.1 Finite Element Analysis

There exists many physical phenomena around the world and they are mostly described by partial differential equations. However, it is almost impossible to the solve partial differential equations analytically in an arbitrary domain [18]. The Finite Element Analysis(FEA) is one of the numerical methods to solve the partial differential equation via a linear system equation. It was first derived for structural problems and expanded to heat transfer, fluid flow, mass transfer, etc.

2.1.1 Variational Method

In this thesis, since an implementation of IGA will be assumed as a two-dimensional linear elasticity problem, variational method will be discussed and utilized for both finite element and isogeometric formulations.

Strain Energy and Potential Energy

By the definition of the strain energy density u, it can be written in

$$u = \frac{1}{2}(\sigma_x \epsilon_x + \sigma_y \epsilon_y + \tau_{xy}\gamma_{xy}) = \frac{1}{2}\boldsymbol{\epsilon}^T \boldsymbol{\sigma} \tag{2.1}$$

where

$$\begin{aligned} \boldsymbol{\epsilon} &= [\epsilon_x \quad \epsilon_y \quad \epsilon_{xy}] \\ \boldsymbol{\sigma} &= [\sigma_x \quad \sigma_y \quad \sigma_{xy}] \end{aligned} \tag{2.2}$$

and T represents a transpose of vector.

Thus, the strain energy can be obtained by taking the integral of (2.1) throughout the domain of interest Ω in the form

$$\begin{aligned} U &= \frac{1}{2}\int_{\Omega} \boldsymbol{\epsilon}^T \boldsymbol{\sigma}\, d\Omega \\ &= \frac{1}{2}\int_{\Omega} \boldsymbol{\epsilon}^T [\overline{\mathbf{Q}}]\boldsymbol{\epsilon}\, d\Omega \end{aligned} \tag{2.3}$$

where $\overline{\mathbf{Q}}$ is a stiffness matrix.

In addition, the potential energies for external forces in static case, concentrated force, traction, and body force can be expressed by integrating the products of displacement $\mathbf{d} = [u_1, v_1, u_2, v_2, ..., v_n, v_n]^T$ where n is number of node per element and external forces such that

$$\Omega^c = -\sum_{i=1}^{n} \mathbf{d}^T \mathbf{F}, \quad n : \text{number of nodes per element}, \quad \mathbf{F} = \begin{Bmatrix} F_{1x} \\ F_{1y} \\ \vdots \\ F_{nx} \\ F_{ny} \end{Bmatrix} \tag{2.4}$$

$$\Omega^t = -\int_{\Gamma_t} \mathbf{d}^T \mathbf{T}\, d\Gamma_t, \quad \mathbf{T} = \begin{Bmatrix} T_x \\ T_y \end{Bmatrix} \tag{2.5}$$

$$\Omega^b = -\int_{\Omega} \mathbf{d}^T \mathbf{b}\, d\Omega, \quad \mathbf{b} = \begin{Bmatrix} b_x \\ b_y \end{Bmatrix} \tag{2.6}$$

Thus, the total potential energy Π_p of the system can be obtained by adding all together (2.3-2.6).

$$\begin{aligned} \Pi_p &= U + \Omega \\ &= U + \Omega^c + \Omega^s + \Omega^b \end{aligned} \tag{2.7}$$

Minimum Potential Energy Principle

Assuming a linear elastic system of all kinematically admissible displacement solution and satisfying the equilibrium equations, the minimum potential energy principle may be applied

such that

$$\delta(\Pi_p) = \delta(U + \Omega) = 0 \tag{2.8}$$

and this implies that

$$h \int_A \mathbf{B}^T \overline{\mathbf{Q}} \mathbf{B} \, dA\{d\} = \mathbf{f}^{tot}, \tag{2.9}$$

where h is a uniform thickness, $\mathbf{f}^{tot}$ is a total external force, and

$$\mathbf{B} = \begin{bmatrix} N_{1,x} & 0 & N_{2,x} & 0 & \cdots & N_{n,x} & 0 \\ 0 & N_{1,y} & 0 & N_{2,y} & \cdots & 0 & N_{n,y} \\ N_{1,y} & N_{1,x} & N_{2,y} & N_{2,x} & \cdots & N_{n,y} & N_{n,x} \end{bmatrix} \tag{2.10}$$

Therefore, the liner system of equation can be simplified by (2.9) such that

$$\mathbf{Kd} = \mathbf{f}, \tag{2.11}$$

which is a linear system.

2.1.2 Elasticity Matrix for Curvilinear Transverse Isotrophy

The material is referred to as transversely isotropic if the material has three pales of symmetry [20]. Suppose that x_1, x_2, x_3 are the axis tangent to a fiber direction, the axis perpendicular to a fiber direction and the axis normal to x_1-x_2 plane, respectively. Then, the compliance matrix in terms of the engineering constants can be written in the form

$$\mathbf{S} = \begin{bmatrix} \frac{1}{E_1} & -\frac{\nu_{21}}{E_2} & -\frac{\nu_{21}}{E_2} & 0 & 0 & 0 \\ -\frac{\nu_{12}}{E_1} & \frac{1}{E_2} & -\frac{\nu_{32}}{E_2} & 0 & 0 & 0 \\ -\frac{\nu_{12}}{E_1} & -\frac{\nu_{23}}{E_2} & \frac{1}{E_2} & 0 & 0 & 0 \\ 0 & 0 & 0 & \frac{2(1+\nu_{23})}{E_2} & 0 & 0 \\ 0 & 0 & 0 & 0 & \frac{1}{G_{13}} & 0 \\ 0 & 0 & 0 & 0 & 0 & \frac{1}{G_{13}} \end{bmatrix}. \tag{2.12}$$

where E_1,E_2, and G_{13} are Young's modulus in the x_1, x_2, and shear modulus in the x_1-x_3 plane, respectively, and ν_{12}, ν_{21}, ν_{23}, and ν_{32} are Poison's ratio in the x_1-x_2 plane, x_2-x_1 plane, x_2-x_3 plane, and x_3-x_2 plane respectively.

Assuming plane-stress condition, the stress in the x_3-direction and both out-of-plane shear stress components are all zeros:

$$\sigma_3 = 0, \quad \tau_{23} = 0, \quad \tau_{13} = 0. \tag{2.13}$$

Thus, the stress-strain relationship can be expressed by substituting (2.13) and inverting (2.12) in the form

$$\begin{bmatrix} \sigma_1 \\ \sigma_2 \\ \tau_{12} \end{bmatrix} = \begin{bmatrix} Q_{11} & Q_{12} & 0 \\ Q_{12} & Q_{22} & 0 \\ 0 & 0 & Q_{66} \end{bmatrix} \begin{bmatrix} \epsilon_1 \\ \epsilon_2 \\ \gamma_{12} \end{bmatrix}, \tag{2.14}$$

where

$$\begin{aligned} Q_{11} &= \frac{E_1}{1 - \nu_{12}\nu_{21}} \\ Q_{22} &= \frac{E_2}{1 - \nu_{12}\nu_{21}} \\ Q_{12} &= \frac{\nu_{12}E_2}{1 - \nu_{12}\nu_{21}} \\ Q_{66} &= G_{12}, \quad G_{12} = G_{13}. \end{aligned} \quad . \tag{2.15}$$

Applying the transformation matrix $\mathbf{T}_\sigma$ and $\mathbf{T}_\epsilon$, the stress-strain relationship in the global coordinate can be represented in

$$\begin{bmatrix} \sigma_x \\ \sigma_y \\ \tau_{xy} \end{bmatrix} = \mathbf{T}_\sigma^T \begin{bmatrix} Q_{11} & Q_{12} & 0 \\ Q_{12} & Q_{22} & 0 \\ 0 & 0 & Q_{66} \end{bmatrix} \mathbf{T}_\epsilon \begin{bmatrix} \epsilon_x \\ \epsilon_y \\ \gamma_{xy} \end{bmatrix} \tag{2.16}$$

where

$$\mathbf{T}_\sigma = \begin{bmatrix} \cos^2\theta & \sin^2\theta & 2\cos\theta\sin\theta \\ \sin^2\theta & \cos^2\theta & -2\cos\theta\sin\theta \\ -\cos\theta\sin\theta & \cos\theta\sin\theta & \cos^2\theta - \sin^2\theta \end{bmatrix}, \tag{2.17}$$

and

$$\mathbf{T}_\epsilon = \begin{bmatrix} \cos^2\theta & \sin^2\theta & \cos\theta\sin\theta \\ \sin^2\theta & \cos^2\theta & -\cos\theta\sin\theta \\ -2\cos\theta\sin\theta & 2\cos\theta\sin\theta & \cos^2\theta - \sin^2\theta \end{bmatrix}, \tag{2.18}$$

θ represents the fiber orientation measured from the global x-axis.

Thus, the rotated elasticity matrix $\overline{\mathbf{C}}$ can be written in

$$\overline{\mathbf{C}} = \mathbf{T}_{\sigma}^{T}\mathbf{C}\mathbf{T}_{\epsilon} \tag{2.19}$$

where

$$\mathbf{C} = \begin{bmatrix} Q_{11} & Q_{12} & 0 \\ Q_{12} & Q_{22} & 0 \\ 0 & 0 & Q_{66} \end{bmatrix}. \tag{2.20}$$

2.2 Non-uniform Rational B-spline

2.2.1 Knot Vector and B-spline

In NURBS-based Isogeometric Analysis, the basis functions are defined by NURBS basis functions, which are constructed by knot vector such that

$$\Xi = \Big[\xi_1, \xi_2, \xi_3, \cdots, \xi_{n+p+1}\Big], \quad \xi_i \in \mathbb{R}, \tag{2.21}$$

ξ_i is the i^{th} knot, i is the knot index such that $i = 1, 2, 3, \cdots, n + p + 1$, p is the polynomial order, and n is the number of basis functions used to construct B-spline curve. The knot vector is a non-decreasing set of coordinates in the parameter space. The knots partition the parameter domain into elements, called knot spans. A knot vector refereed to as uniform if a knot vector have equally spaced knot spans each in parametric space. If a knot vector does not have equally spaced knot spans, it is referred to as non-uniform. Knot vector may be called open if the multiplicity of the first and the last knots is $p + 1$. If not, it is said to be closed.

2.2.2 B-spline Function

Given a knot vector in parameter space defined in (2.21), then the i-th B-spline basis function of order p, denoted by $N_{i,p}(\xi)$ is defined as

for $p = 0$:

$$N_{i,0}(\xi) = \begin{cases} 1 & \text{if } \xi_i \leq \xi < \xi_{i+1}, \\ 0 & \text{otherwise,} \end{cases} \tag{2.22}$$

for $p = 1, 2, 3, \cdots$,

$$N_{i,p}(\xi) = \frac{\xi - \xi_i}{\xi_{i+p} - \xi_i} N_{i,p-1}(\xi) + \frac{\xi_{i+p+1} - \xi}{\xi_{i+p+1} - \xi_{i+1}} N_{i+1,p-1}(\xi). \tag{2.23}$$

This function is called Cox-de Boor recursion formula [8, 9, 5]. Figure 2 shows the results of B-spline functions with order $p = 0, 1, 2$ using the uniform knot vector. As can be noted in the figure, B-spline functions have compact support, which means they are zero outside the corresponding interval. B-spline function also has the partition of unity property such that

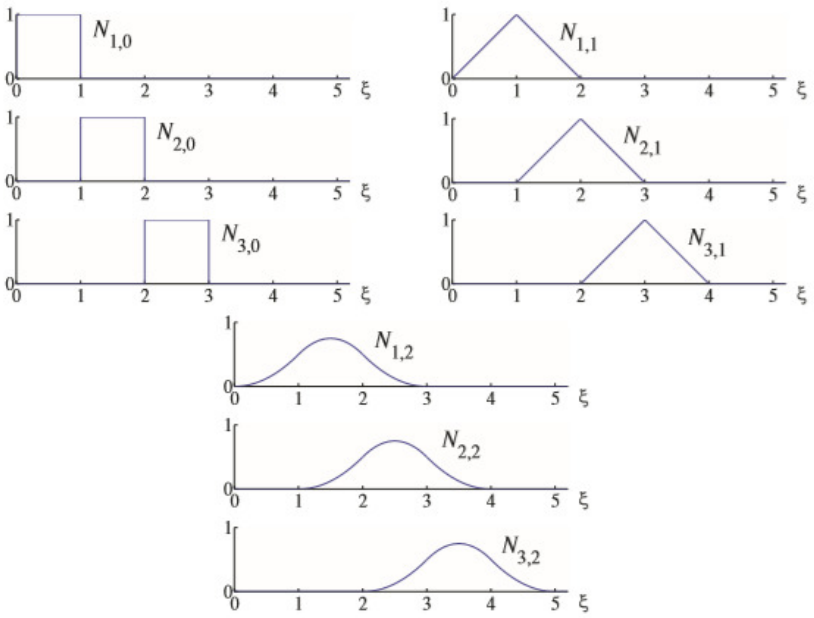

Figure 2.1: B-spline basis functions with order $p = 0, 1, 2$ for uniform knot vector $\Xi = [0, 1, 2, 3, 4, 5, \cdots]$(adapted from [4]).

$$\sum_{i=1}^{n} N_{i,p}(\xi) = 1 \quad \forall \xi. \tag{2.24}$$

2.2.3 Derivative of B-spline function

Let $N_{i,p}(\xi)$ be p-th order B-spline function defined by the knot vector $\Xi = [\xi_1, \cdots, \xi_{n+p+1}]$. The derivative of B-spline function $\frac{d}{d\xi}N_{i,p}(\xi)$ is calculated recursively as

$$\frac{d}{d\xi}N_{i,p}(\xi) = \frac{p}{\xi_{i+p} - \xi_i}N_{i,p-1}(\xi) - \frac{p}{\xi_{i+p+1} - \xi_{i+1}}N_{i+1,p-1}(\xi). \tag{2.25}$$

This can be proven by mathematical induction [27]. The k-th derivative of the B-spline function, denoted by $N_{i,p}^{(k)}$ also can be computed by

$$N_{i,p}^{(k)} = p\left(\frac{N_{i,p-1}^{(k-1)}}{\xi_{i+p} - \xi_i} - \frac{N_{i+1,p-1}^{(k-1)}}{\xi_{i+p+1} - \xi_{i+1}}\right). \tag{2.26}$$

Alternatively, the $k-th$ derivative may be computed in terms of B-spline functions such that

$$N_{i,p}^{(k)} = \frac{p!}{(p-k)!}\sum_{j=0}^{k} a_{k,j}N_{i+j,p-k}(\xi) \tag{2.27}$$

where

$$\begin{aligned} a_{0,0} &= 1 \\ a_{k,0} &= \frac{a_{k-1,0}}{\xi_{i+p-k+1} - \xi_i} \\ a_{k,j} &= \frac{a_{k-1,j} - a_{k-1,j-1}}{\xi_{i+p+j-k+1} - \xi_{i+j}} \quad j = 1, 2, \cdots, k-1 \\ a_{k,k} &= \frac{-a_{k-1,k-1}}{\xi_{i+p+1} - \xi_{i+k}}. \end{aligned} \tag{2.28}$$

2.2.4 B-spline Curve and Surface

B-spline curves are constructed by taking linear combinations of B-spline basis functions like in a classical FEM. The coefficients of each B-spline basis functions are referred to as control points. Unlike Lagrangian polynomial functions in a conventional FEA, the control points do not always interpolate as nodes.

Given n basis functions $N_{i,p}$, where $i = 1, 2, \cdots, n$ and corresponding control points $\mathbb{P}_i \in \mathbb{R}$, where $i = 1, 2, \cdots, n$, the B-spline curve is defined by

$$\mathbf{C}(\xi) = \sum_{i=1}^{n} N_{i,p}(\xi)\mathbb{P}_i. \tag{2.29}$$

In a same manner, the B-spline surface is also defined by giving a control net $\mathbb{P}_{i,j}$, where $i = 1, 2, ..., n, j = 1, 2, ..., m$, polynomial order p and q, and knot vectors $\Xi = [\xi_1, \xi_2, ..., \xi_{n+p+1}]$, and $H = [\eta_1, \eta_2, ..., \eta_{m+q+1}]$, a tensor product B-spline surface is given by

$$\mathbf{S}(\xi, \eta) = \sum_{i=1}^{n} \sum_{j=1}^{m} N_{i,p}(\xi) M_{j,q}(\eta) \mathbb{P}_{i,j}. \tag{2.30}$$

2.2.5 NURBS Basis Function and Surface

Given the knot vector defined in (2.21), the p-th order NURBS function is given by

$$R_i^p(\xi) = \frac{N_{i,p}(\xi)\omega_i}{\sum_{\hat{i}=1}^{n} N_{\hat{i},p}\omega_{\hat{i}}} \tag{2.31}$$

where ω_i is the weights and $N_{i,p}(\xi)$ is B-spline function defined by (2.22) and (2.23). The NURBS functions $R_i^p(\xi)$ are piece-wise rational functions on the knot span $\xi \in [\xi_i, \xi_{i+1})$.

Applying corresponding control points $\mathbb{P}_i$ to the NURBS function (2.31), the NURBS curve can be derived as

$$\mathbf{C}(\xi) = \sum_{i=1}^{n} R_i^p(\xi) \mathbb{P}_i. \tag{2.32}$$

Similarly, we can derive the NURBS basis function and the NURBS surface, respectively,

$$R_{i,j}^{p,q}(\xi, \eta) = \frac{N_{i,p}(\xi) M_{j,q}(\eta) \omega_{i,j}}{\sum_{\hat{i}=1}^{n} \sum_{\hat{j}=1}^{m} N_{\hat{i},p} M_{j,q}(\eta) \omega_{i,j}}, \tag{2.33}$$

$$\mathbf{S}(\xi, \eta) = \sum_{i=1}^{n} \sum_{j=1}^{m} R_{i,j}^{p,q}(\xi) \mathbb{P}_{i,j}. \tag{2.34}$$

where $N_{i,p}(\xi)$ and $M_{j,q}(\eta)$ are p-th B-spline function in ξ-direction and q-th B-spline function in η-direction, respectively, and $\omega_{i,j}$ is weights for the corresponding control points $\mathbb{P}_{i,j}$.

2.2.6 Derivative of NURBS Function

The derivative of NURBS function is simply derived using quotient rule to (2.31) via the derivative of B-spline function (2.25) or (2.27) as

$$\frac{d}{d\xi} R_i^p(\xi) = \omega_i \frac{W(\xi) N'_{i,p}(\xi) - W'(\xi) N_{i,p}(\xi)}{(W(\xi))^2}, \tag{2.35}$$

where $N'_{i,p} \equiv \frac{d}{d\xi} N_{i,p}(\xi)$ and

$$W'(\xi) = \sum_{\hat{i}=1}^{n} N'_{\hat{i},p}(\xi)\omega_{\hat{i}}. \tag{2.36}$$

2.3 IGA Framework

In a geometrical modeling process, the concept of NURBS can be utilized, which means the geometry may be generated by a tensor product of NURBS basis functions (2.31) and control points each knot span. Unlike a conventional FEA, once the geometry is decided by the knot vectors, the mesh is also automatically generated by the use of a knot vector.

In the process of analysis, variational method can be used to solve the partial differential equation. The NURBS basis functions can be applied as basis/interpolation functions instead of a classical basis function e.g. Lagrange polynomials. The element equations of linear system can be evaluated by Gaussian quadrature. Once the evaluation has been completed, the assemble will be implemented to build a global element equation.

2.3.1 Mesh Generation

In NURBS-based Isogeometric Analysis, meshing process is straightforward procedure. Once the geometry is defined, knot vectors, control points with corresponding weights and the order of NURBS basis function can be extracted. Then, the mesh can be automatically generated by the using these properties.

In NURBS-based Isogeometric Analysis, the mesh itself is defined by knot spans $\xi \in [\xi_i, \xi_{i+1})$ created by the knot vector Ξ (2.21), meaning that the mesh is partitions of the tensor product of NURBS basis functions and control points with corresponding weights each knot span $\xi \in [\xi_i, \xi_{i+1})$.

Figure 2.2 represents the element meshes in the case of one-dimensional(figure 2.2a) and two-dimensional(figure 2.2b), respectively. The blue squares show their knots, and they partition the geometry into knot span or so called element. Their geometric data are also shown in table 2.1 and 2.2 for one- and two-dimensional cases, respectively. All the weights

are assigned as one in this two cases.

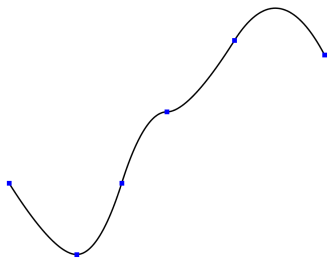

(a) NURBS-based Isogeometric mesh using the knot vector $\Xi = [0, 0, 0, 0.2, 0.5, 0.75, 1, 1, 1]$ and control points shown in table 2.1

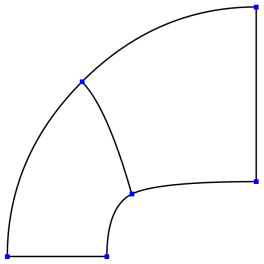

(b) NURBS-based Isogeometric mesh using the knot vectors $\Xi = [0, 0, 0, 0.5, 1, 1, 1]$, $H = [0, 0, 0, 1, 1, 1]$ and control points shown in table 2.2

Figure 2.2: Examples of NURBS-based Isogeometric Mesh(adapted from [4]).

Table 2.1: Control Points with corresponding weights (third components) of figure 2.2a (adapted from [4]).

	i=1	i=2	i=3	i=4	i=5	i=6	i=7	i=8
j=1	(0,1,1)	(1,0,1)	(2,0,1)	(3,2,1)	(4,2,1)	(5,3,1)	(6,4,1)	(7,2.8,1)

2.3.2 Refinement

In NURBS-based Isogeometric Analysis, the mesh of the geometry may be generated, automatically. As mentioned before, one of the advantages of NURBS basis functions is that it is flexible to enrich the basis functions e.g. the order of basis function, the number of the basis functions, etc. Unlike a conventional FEA, it is relatively easy not only to elevate the

Table 2.2: Control Points with corresponding weights (third components) of figure 2.2b (adapted from [4]).

	i=1	i=2	i=3	i=4
j=1	(0,0,1)	(0,1,1)	(1,1.5,1)	(3,1.5,1)
j=2	(-1,0,1)	(-1,2,1)	(1,4,1)	(3,4,1)
j=3	(-2,0,1)	(-2,2,1)	(1,5,1)	(3,5,1)

order of NURBS basis function but also to control the mesh size and continuity of the basis as well [4].

Knot Insertion

To have an enriched basis function or create a finer mesh for the stress analysis, knot insertion can be implemented. Knot can be inserted into the knot vector without any changes in geometry at all.

Given that the NURBS curve $\mathbf{C}(\xi) = \sum_{i=1}^{n} N_{i,p}(\xi)\mathbb{P}_i$ on the knot vector $\Xi = [\xi_1, \xi_2, ..., \xi_n]$. Let $\overline{\xi} \in [\xi_k, \xi_{k+1})$ be inserted into the knot vector Ξ, then create the new knot vector $\overline{\Xi}$ such that

$$\overline{\Xi} = [\overline{\xi}_1 = \xi_1, ..., \overline{\xi}_k = \xi_k, ..., \overline{\xi}_{k+1} = \overline{\xi}, ..., \overline{\xi}_{k+2} = \xi_{k+1}, ..., \overline{\xi}_{n+1} = \xi_n]. \tag{2.37}$$

Because $\Xi \subset \overline{\Xi}$, the NURBS curve inserted by $\overline{\xi}$ can be represented by

$$\mathbf{C}(\xi) = \sum_{i=1}^{n+1} \overline{N}_{i,p}(\xi)\mathbb{Q}_i \qquad \text{on} \qquad \overline{\Xi}. \tag{2.38}$$

where $\overline{N}_{i,p}$ are p-th degree basis function on $\overline{\Xi}$ and $\mathbb{Q}_i$ are the corresponding control points.

Since the geometry of the NURBS curves are exactly same before and after knot inserted, we can equate the both NURBS curves defined above such that

$$\sum_{i=1}^{n} N_{i,p}(\xi)\mathbb{P}_i = \sum_{i=1}^{n+1} \overline{N}_{i,p}(\xi)\mathbb{Q}_i \tag{2.39}$$

and this enable us to find out the new control points $\mathbb{Q}_i$ such that

$$\mathbb{Q}_i = \alpha_i \mathbb{P}_i + (1 - \alpha_i)\mathbb{P}_{i-1} \tag{2.40}$$

where

$$\alpha_i = \begin{cases} 1 & i \leq k - p \\ \frac{\bar{\xi} - \xi_i}{\xi_{i+p} - \xi_i} & k - p + 1 \leq i \leq k \\ 0 & i \geq k + 1 \end{cases} \tag{2.41}$$

The proof of this can be referred in [27].

The figure 2.3 shows the example of refinement using knot insertion (2.40). The knot vectors and the corresponding control points are shown in table 2.2 and 2.3. The knot insertion is implemented uniformly for each knot span in both ξ- and η- directions.

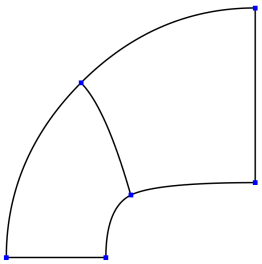

(a) NURBS-based Isogeometric mesh using the knot vectors $\Xi = [0, 0, 0, 0.5, 1, 1, 1]$, $H = [0, 0, 0, 1, 1, 1]$ and control points shown in table 2.2

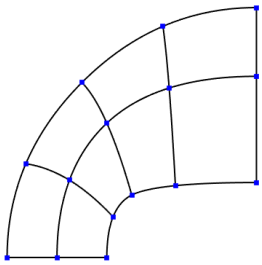

(b) NURBS-based Isogeometric mesh using the knot vectors $\Xi = [0, 0, 0, 0.2, 0.5, 0.75, 1, 1, 1]$, $H = [0, 0, 0, 0.5, 1, 1, 1]$ and control points shown in table 2.3

Figure 2.3: NURBS-based Isogeometric Mesh Refinement using the knot insertion(adapted from [4])

Table 2.3: Control Points with corresponding weights (third components) of figure 2.3b (adapted from [4])

	i=1	i=2	i=3	i=4	i=5	i=6
j=1	(0,0,1)	(0,0.5,1)	(0.25,1.125,1)	(0.75,1.375,1)	(2,1.5,1)	(3,1.5,1)
j=2	(-0.5,0,1)	(-0.5,0.75,1)	(-0.125,1.8125,1)	(0.625,2.4375,1)	(2,2.75,1)	(3,2.75,1)
j=3	(-1.5,0,1)	(-1.5,1,1)	(-0.875,2.625,1)	(0.375,3.875,1)	(2,4.5,1)	(3,4.5,1)
j=4	(-2,0,1)	(-2,1,1)	(-1.25,2.75,1)	(0.25,4.25,1)	(2,5,1)	(3,5,1)

Order Elevation

Order elevation is the one of the advantages to use NURBS basis functions. Order elevation can be implemented only by increasing the multiplicity of the knots but adding new knots in order to raise the polynomial order of the NURBS basis function so that we can control the continuity of the basis function.

The control points after t-degree elevations $\mathbb{P}_i^t$ can be derived as

$$\mathbb{P}_i^t = \sum_{j=max(0,i-t)}^{min(p,i)} \frac{\binom{p}{j}\binom{t}{i-j}}{\binom{p+t}{i}} \mathbb{P}_j, \qquad i = 0, ..., p+t \tag{2.42}$$

using the notation $\binom{p}{i} = \frac{p!}{i!(p-i)!}$. Full derivation of the order elevated control points can be cited in [27].

The figure 2.4 represents the original NURBS curve(2.4a) and the refined NURBS curve(2.4b), respectively. The red dots show the control points. The multiplicity of the knots m_i is increased by adding same knot and calculated by (2.42).

The figure 2.5 shows the B-spline basis functions for the quadratic polynomial order (2.5a) and for the cubic polynomial order (2.5b), respectively. Defining that B-spline basis

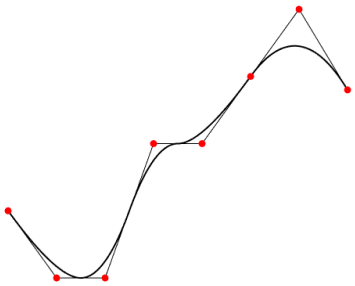

(a) NURBS curve without refinements using the knot vector $\Xi = [0, 0, 0, 0.2, 0.4, 0.6, 0.8, 0.8, 1, 1, 1]$ and control points shown in table 2.1

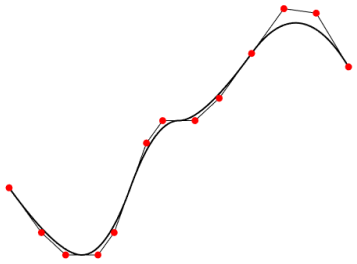

(b) NURBS curve with refinement using the refined knot vector $\Xi = [0, 0, 0, 0, 0.2, 0.2, 0.4, 0.4, 0.6, 0.6, 0.8, 0.8, 0.8, 1, 1, 1, 1]$ and control points shown in table 2.4

Figure 2.4: NURBS curves with refinement using order elevation (adapted from [4])

Table 2.4: Control Points with corresponding weights (third components) of figure 2.4b (adapted from [4]).

	i=1	i=2	i=3	i=4	i=5
j=1	(0,1,1)	(0.667,0.333,1)	(1.167,0,1)	(1.833,0,1)	(2.167,0.333,1)

	i=6	i=7	i=8	i=9	i=10
j=1	(2.833,1.667,1)	(3.167,2,1)	(3.833,2,1)	(4.333,2.333,1)	(5,3,1)

	i=11	i=12	i=13
j=1	(5.667,3.667,1)	(6.333,3.6,1)	(7,2.8,1)

functions has C^n continuity if $n = p - m_i$, where m_i is the multiplicity of the knot, B-spline basis functions are C^{-1} continuity at $\xi = 0, 5$, however, they are C^1 continuity elsewhere except $\xi = 4$. In addition, the B-spline basis functions have C^0 continuity at $\xi = 4$ due to the high multiplicities. It is useful to control the continuity of the B-spline basis functions and to enrich the NURBS basis function by the use of knot insertion and degree elevation, especially in the case of discontinuous modeling e.g. crack analysis and surface interfaces [30, 25].

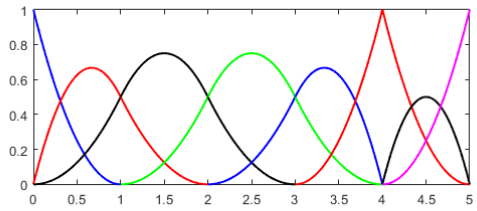

(a) Quadratic B-spline basis functions by the knot vector $\Xi = [0, 0, 0, 1, 2, 3, 4, 4, 5, 5, 5]$

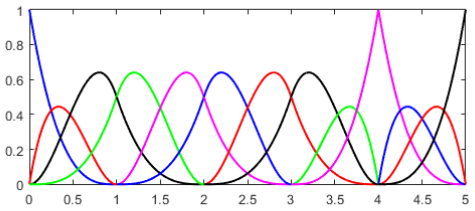

(b) Cubic B-spline basis functions by the knot vector $\Xi = [0, 0, 0, 0, 1, 1, 2, 2, 3, 3, 4, 4, 4, 1, 1, 1, 1]$

Figure 2.5: Refined B-spline curves using order elevation(adapted from [4])

2.3.3 Assembling

The assembling process in IGA follows the same algorithm as in a classical FEA. To solve the partial differential equations, it is common to discretize the domain into elements. Each element defined by the knot spans has non-zero NURBS basis functions, so it is necessary to loop over the elements to get access to each NURBS basis function. Then, from the derived linear system of equations (2.9), the local stiffness matrices and force vectors may

be computed for each element. The local stiffness matrix and force vector are also referred to as element stiffness matrix and force vector.

When evaluating the local stiffness matrix and force vector, Gaussian quadrature has been chosen. Let Ω, $\hat{\Omega}$, and $\tilde{\Omega}$ be physical space, parameter space, and parent space, respectively. Each element is defined in physical domain Ω^e, and it can be mapped into parameter space $\hat{\Omega}^e$. Then, the domain in parameter space $\hat{\Omega}^e$ need to be mapped into parent domain $\tilde{\Omega}^e \in [-1, 1]^d$, where d is the dimension of the element in order to evaluate each element equation. Figure 2.6 represents the whole picture of the integration using the maps among the three spaces, parameter, physical, and parent space.

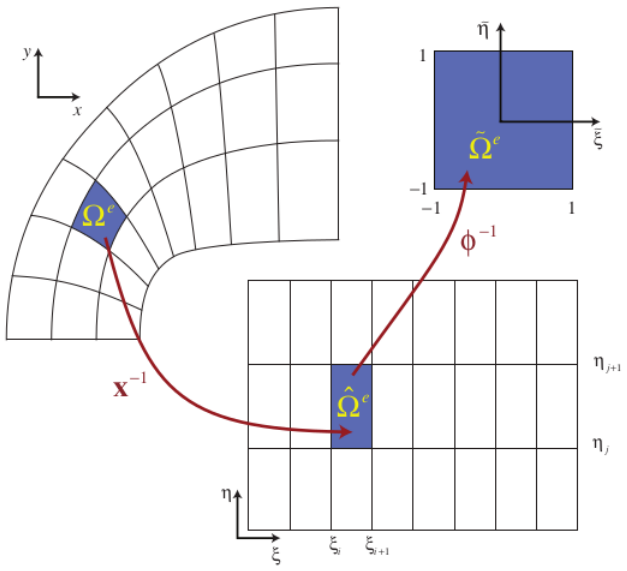

Figure 2.6: The whole picture of integration using Gaussian quadrature on each element(adapted from [4]).

Once the element stiffness matrices and force vectors are computed for each element, they have to be scattered into the global element equation, which means that locally computed stiffness and forces must be place in global system like in a conventional FEM. This routine will be explained in more detail in chapter 3.

2.3.4 Formulation of a Linear System as NURBS basis

The theoretical framework of NURBS-based Isogeometric Analysis, especially in the formulation of a linear system is very similar to a classical FEA framework introduced in section 2.1. Since an implementation of IGA will be used for two-dimensional linear elasticity problem in this thesis, the variational method can be applied to derive the system of equations.

Potential Energy

The potential energy over the domain of interest Ω can be written using (2.1 and 2.2) in the form

$$U = \frac{1}{2}\int_{\Omega} \boldsymbol{\epsilon}^T \overline{\mathbf{C}} \boldsymbol{\epsilon}\, d\Omega \tag{2.43}$$

where $\overline{\mathbf{C}}$ is defined by (2.19), which is rotated by θ measured from the global x-axis.

For the potential energy Ω, consider that three different external forces in a two-dimensional elasticity problem, concentrated forces $\mathbf{f}^c$, surface forces $\mathbf{f}^t$, and body forces $\mathbf{f}^b$. These potential energies can be calculated by integrating the product of displacement and external forces and derived in (2.4-2.6), and $\mathbf{d}$ is denoted as a control variable in this isogeometric formulation

Minimum Potential Energy Principle

The displacement field $\mathbf{u}$ can be expressed by the use of the NURBS basis functions $\mathbf{R}$ and the corresponding control variable $\mathbf{d}$ in the form

$$\mathbf{u} = \mathbf{R}\mathbf{d}. \tag{2.44}$$

where

$$\mathbf{R} = \begin{bmatrix} R_1 & 0 & R_2 & 0 & \cdots & R_n & 0 \\ 0 & R_1 & 0 & R_2 & \cdots & 0 & R_n \end{bmatrix}, \tag{2.45}$$

and

$$\mathbf{d} = \begin{bmatrix} x_1 & y_1 & x_2 & y_2 & ... & x_n & y_n \end{bmatrix}^T. \tag{2.46}$$

n is a number of NURBS basis functions per element.

By the definition of strain, we can re-write the strain in terms of the NURBS basis functions and the corresponding control variable such that

$$\boldsymbol{\epsilon} = \frac{d\mathbf{u}}{d\mathbf{x}} = \frac{d}{d\mathbf{x}}\mathbf{R}\boldsymbol{d} = \mathbf{B}\boldsymbol{d}, \tag{2.47}$$

where $\mathbf{B}$ is referred to as strain-displacement matrix and represented in the form

$$\mathbf{B} = \begin{bmatrix} R_{1,x} & 0 & R_{2,x} & 0 & \cdots & R_{n,x} & 0 \\ 0 & R_{1,y} & 0 & R_{2,y} & \cdots & 0 & R_{n,y} \\ R_{1,y} & R_{1,x} & R_{2,y} & R_{2,x} & \cdots & R_{n,y} & R_{n,x} \end{bmatrix}. \tag{2.48}$$

Utilizing (2.47), we can simplify the (2.43) such that

$$U = \frac{h}{2}\mathbf{d}^T \int_A \mathbf{B}^T \overline{\mathbf{C}}\mathbf{B}\, dA\mathbf{d}. \tag{2.49}$$

where h is a uniform thickness.

Therefore, the derivative of strain energy with respect to $\mathbf{d}$ can be expressed in

$$\frac{\partial U}{\partial \mathbf{d}} = h * I_{n\times n} * \int_A \mathbf{B}^T \overline{\mathbf{C}}\mathbf{B}\, dA * \mathbf{d}. \tag{2.50}$$

In a similar manner, we can obtain the derivatives of the external forces (2.4-2.6) with respect to the control variable $\mathbf{d}$ and they are

$$\frac{\partial \Omega^c}{\partial \mathbf{d}} = -I_{n\times n}\left\{f_{1x}, f_{1y}, \cdots, f_{nx}, f_{ny}\right\}^T, \tag{2.51}$$

$$\frac{\partial \Omega^t}{\partial \mathbf{d}} = -I_{n\times n}\int_{\Gamma_t} \mathbf{R}^T\mathbf{T}\, d\Gamma_t, \tag{2.52}$$

$$\frac{\partial \Omega^b}{\partial \mathbf{d}} = -h * I_{n\times n} * \int_A \mathbf{R}^T\mathbf{b}\, dA, \tag{2.53}$$

Letting concentrated force vector, surface force vector, and body force vector be $\mathbf{f}^c, \mathbf{f}^t, \mathbf{f}^b$, respectively, the total force vector $\mathbf{f}^{tot}$ can be expressed in

$$\mathbf{f}^{tot} = \mathbf{f}^c + \mathbf{f}^t + \mathbf{f}^b = \begin{Bmatrix} f^c_{1x} \\ f^c_{1y} \\ \vdots \\ f^c_{nx} \\ f^c_{ny} \end{Bmatrix} + \begin{Bmatrix} f^t_{1x} \\ f^t_{1y} \\ \vdots \\ f^t_{nx} \\ f^t_{ny} \end{Bmatrix} + \begin{Bmatrix} f^b_{1x} \\ f^b_{1y} \\ \vdots \\ f^b_{nx} \\ f^b_{ny} \end{Bmatrix}. \tag{2.54}$$

where each external force is extracted from (2.51-2.53).

Applying the minimum potential energy principal, we can obtain the following linear system

$$\delta(\Pi_p) = \delta(U + \Omega) = 0, \tag{2.55}$$

which implies that

$$h \int_A \mathbf{B}^T \overline{\mathbf{C}} \mathbf{B} \, dA * \mathbf{d} = \mathbf{f}^{tot}. \tag{2.56}$$

by (2.9, 2.10, 2.19 and 2.54).

Therefore, the linear system using NURBS basis function can be simplified as

$$\mathbf{K}\mathbf{d} = \mathbf{f}^{tot} \tag{2.57}$$

2.3.5 Isogeometric Formulation

Discretisation

Discritisation of the NURBS and B-splines have been introduced in section 2.2 as a function of ξ and η, which are parameter space defined in (2.33). For the analysis, the geometry in parent domain can be defined as

$$\mathbf{x}(\tilde{\xi}) = \sum_{a=1}^{n} R_a^e(\tilde{\xi}) \mathbf{P}_a^e \tag{2.58}$$

where a is a local basis function number at an element e, and n is a number of support of the local basis functions, and $R_a^e(\tilde{\xi})$ and $\mathbf{P}_a^e$ are local basis function at an element e and corresponding control points for the basis functions, respectively.

Thus, the solution space $\mathbf{u}$, which is the solution of the PDEs can be described by the form

$$\mathbf{u}^e(\tilde{\xi}) = \sum_{a=1}^{n} R_a^e(\tilde{\xi}) \mathbf{d}_a^e \tag{2.59}$$

where $\mathbf{d}_a^e$ is a nodal or control variable at local basis function a each element e.

Mapping and Gradient

Although the NURBS basis functions are defined in parameter space, the element stiffness matrix using Gaussian quadrature should be evaluated in parent space. Thus, two mappings among parameter, parent, and physical spaces (figure 1.4) may be introduced for the element defined by knot span $[\xi_i, \xi_{i+1}) \otimes [\eta_i, \eta_{i+1})$. The mapping from parent space to parameter space can be written in

$$\begin{aligned} \xi &= \frac{1}{2}[(\xi_{i+1} - \xi_i)\tilde{\xi} + (\xi_{i+1} - \xi_i)] \\ \eta &= \frac{1}{2}[(\eta_{i+1} - \eta_i)\tilde{\eta} + (\eta_{i+1} - \eta_i)] \end{aligned} \tag{2.60}$$

and the associated Jacobian $\mathbf{J}_{\tilde{\xi}}$ and the determinant $J_{\tilde{\xi}}$ are expressed respectively in

$$\mathbf{J}_{\tilde{\xi}} = \begin{bmatrix} \xi_{,\tilde{\xi}} & \xi_{,\tilde{\eta}} \\ \eta_{,\tilde{\xi}} & \eta_{,\tilde{\eta}} \end{bmatrix} \tag{2.61}$$

and

$$J_{\tilde{\xi}} = \frac{1}{4}(\xi_{i+1} - \xi_i)(\eta_{i+1} - \eta_i). \tag{2.62}$$

In addition to the mapping from parent to parameter space, it is also necessary to derive the Jacobian $\mathbf{J}_\xi$ between physical and parameter and the determinant J_ξ. Using the definition of the derivative of the NURBS basis function defined in (2.35), the derivatives of NURBS basis functions with respect to parameter space ξ and η can be expressed in

$$\mathbf{R}_{,\boldsymbol{\xi}} = \begin{bmatrix} R_{1,\xi} & R_{2,\xi} & ... & R_{n,\xi} \\ R_{1,\eta} & R_{2,\eta} & ... & R_{n,\eta} \end{bmatrix} \tag{2.63}$$

with the corresponding control points

$$\mathbf{P} = \begin{bmatrix} x_1 & y_1 \\ x_2 & y_2 \\ \vdots & \vdots \\ x_n & y_n \end{bmatrix}, \tag{2.64}$$

Thus, the Jacobian J_ξ can be written in

$$\mathbf{J}_\xi = \mathbf{P}^T \mathbf{R}_{,\boldsymbol{\xi}}^T = \begin{bmatrix} x_{,\xi} & x_{,\eta} \\ y_{,\xi} & y_{,\eta} \end{bmatrix} \tag{2.65}$$

and the associated determinant J_ξ is then expressed in

$$J_\xi = x_{,\xi}\, y_{,\eta} - x_{,\eta}\, y_{,\xi}\,. \tag{2.66}$$

To calculate the element stiffness derived in (2.57), strain-displacement matrix $\mathbf{B}$ (2.10) in terms of the derivative of NURBS basis functions with respect to x and y such that

$$\mathbf{R}_{,\mathbf{x}} = \begin{bmatrix} R_{1,\xi} & R_{1,\eta} \\ R_{2,\xi} & R_{2,\eta} \\ \vdots & \vdots \\ R_{n,\xi} & R_{n,\eta} \end{bmatrix} \begin{bmatrix} \xi_{,x} \; \xi_{,y} \\ \eta_{,x} \; \eta_{,y} \end{bmatrix} = \mathbf{R}_{,\boldsymbol{\xi}}^{\,T}\, \mathbf{J}_\xi^{-1} \tag{2.67}$$

where the derivative of the NURBS basis function with respect to parameter coordinate can be found in (2.35).

Element Equation

The classic composites reinforced by fibers are always parallel to each fiber so that they are straight and the fiber orientation θ is constant. However, when it comes to the composites reinforced by curvilinear fibers (CTI), it is not necessary to be parallel to each fiber. In this fiber configurations, it is common to analyze on such a material by discretizing curvilinear fiber paths and assign the fiber orientation θ as constant each element [15].

For the sake of more precision, new method to capture the curvilinear fiber paths more precisely will be proposed, that is updating the fiber orientation θ each integration point but each element. Thus, the elasticity stiffness matrix (2.19) varies each integration point in the process of evaluation.

To calculate the element equation, it is necessary to first calculate the strain-displacement matrix and the element stiffness matrix configured with appropriate fiber orientations each integration point. The strain-displacement matrix may be calculated applying the derived

one (2.48) from the minimum potential energy principal such that

$$\mathbf{B} = \begin{bmatrix} R_{1,x} & 0 & R_{2,x} & 0 & \cdots & R_{n,x} & 0 \\ 0 & R_{1,y} & 0 & R_{2,y} & \cdots & 0 & R_{n,y} \\ R_{1,y} & R_{1,x} & R_{2,y} & R_{2,x} & \cdots & R_{n,y} & R_{n,x} \end{bmatrix} \tag{2.68}$$

Note that the spacial derivative of the NURBS basis function is calculated by (2.67).

To calculate the element stiffness matrix, it is necessary to update the stiffness matrix each integration point assuming the use of Gaussian quadrature rule for the evaluation purpose. Each physical coordinate of the Gauss point(integration point) can be expressed by the NURBS basis function $\mathbf{R}$ and the corresponding control point $\mathbf{P}$ such that

$$\mathbf{x} = \mathbf{R}(\boldsymbol{\xi})\mathbf{P} \tag{2.69}$$

where

$$\mathbf{R}(\xi) = \begin{bmatrix} R_1(\boldsymbol{\xi}) & 0 & R_2(\boldsymbol{\xi}) & 0 & ... & R_n(\boldsymbol{\xi}) & 0 \\ 0 & R_1(\boldsymbol{\xi}) & 0 & R_2(\boldsymbol{\xi}) & ... & 0 & R_n(\boldsymbol{\xi}) \end{bmatrix} \tag{2.70}$$

Remind that ξ and η can be calculated by (2.60).

Assume that a function of the physical coordinate ϕ that outputs the fiber orientation θ such that

$$\theta = \phi(x, y), \tag{2.71}$$

then, the element stiffness matrix can be calculated using transformation matrices defined by (2.17 and 2.18) such that

$$\overline{\mathbf{C}} = \mathbf{T}_{\sigma}^{-1}(\theta)\mathbf{C}\mathbf{T}_{\epsilon}(\theta) \tag{2.72}$$

where $\mathbf{C}$ and θ are found in (2.20) and (2.71), respectively.

To evaluate the local stiffness matrix, Gaussian quadrature can be applied. Since our element stiffness matrix is an integration over the domain defined in physical coordinate Ω, it is required to enable it to be suitable domain of the integration. As can be noted in the figure 2.6, the domain in physical coordinate Ω has to be mapped into parent space $\tilde{\Omega}$ via

parameter space $\hat{\Omega}$. Letting $f(\mathbf{x})$ is a function of physical coordinate, then the transformation from that function $f(\mathbf{x})$ into the one in parent domain can be represented by

$$\begin{aligned}\int_{\Omega} f(\mathbf{x})\, d\Omega &= \int_{\hat{\Omega}} f(\boldsymbol{\xi}) J_{\xi}\, d\hat{\Omega} \\ &= \int_{\tilde{\Omega}} f(\tilde{\boldsymbol{\xi}}) J_{\xi} J_{\tilde{\xi}}\, d\tilde{\Omega}\end{aligned} \tag{2.73}$$

where J_{ξ} and $J_{\tilde{\xi}}$ are determinants of the Jacobians and defined by (2.66) and (2.62), respectively.

Therefore, the element stiffness matrix can be derived by (2.56) applying Gaussian quadrature rule such that

$$\begin{aligned}\mathbf{K}^e &= h \int_{\Omega} \mathbf{B}^T \overline{\mathbf{C}} \mathbf{B}\, d\Omega \\ &= h \int_{\tilde{\Omega}} \mathbf{B}^T \overline{\mathbf{C}} \mathbf{B} J_{\xi} J_{\tilde{\xi}}\, d\tilde{\Omega} \\ &= h \sum_{gp=1}^{ngp} \mathbf{B}^T \overline{\mathbf{C}}_{gp} \mathbf{B} J_{\xi} J_{\tilde{\xi}} W_{gp}\end{aligned} \tag{2.74}$$

where $\overline{\mathbf{C}}$ is dependent on the Gauss points gp and W represents the corresponding weights of the ngp Gauss points.

Chapter 3

IMPLEMENTATION OF NURBS-BASED ISOGEOMETRIC ANALYSIS

Both NURBS-based IGA and FEA have first been implemented in Python environment under a linear elasticity problem and plane-stress condition for an isotropic case. Then, the open-source MATLAB IGA code (`https://sourceforge.net/projects/cmcodes/`) provided by V.P. Nguyen *et al.,* 2015 [24] has been utilized in order to focus on the analysis of composites reinforced curvilinear fibers and its optimization study. This open source code is mostly written in MATLAB and has a variety of functions e.g. refinement, visualizations, NURBS basis functions subroutines, etc.

3.1 Isogeometric Analysis in Python Environment

3.1.1 NURBS Basis function Routine

To compute the derivative of the NURBS basis function with respect to parameter space $\boldsymbol{\xi}$, computation of the B-spline basis functions (2.22 and 2.23) at ξ_i is necessary to find out the derivatives of the B-spline functions using (2.27). Once the derivatives of the B-spline functions are found, the derivatives of the NURBS basis function with respect to parameter space can be calculated by (2.35). Piegl and Tiller discuss the following efficient computational method for B-spline functions and the derivatives in [27].

Let n_i be a NURBS coordinate, which means the first index of certain knot span and consider the support of the second-order degree B-spline functions at the NURBS coordinate n_i constructed by $\Xi = [0, 0, 0, 1, 2, 3, 4, 4, 5, 5, 5]$, then there exists three B-spline functions such that

$$N_{n_i-2,2}(\xi) = \frac{\xi - \xi_{n_i-2}}{\xi_{n_i} - \xi_{n_i-2}} N_{n_i-2,1}(\xi) + \frac{\xi_{n_i+1} - \xi}{\xi_{n_i+1} - \xi_{n_i-1}} N_{n_i-1,1}(\xi) \tag{3.1}$$

$$N_{n_i-1,2}(\xi) = \frac{\xi - \xi_{n_i-1}}{\xi_{n_i+1} - \xi_{n_i-1}} N_{n_i-1,1}(\xi) + \frac{\xi_{n_i+2} - \xi}{\xi_{n_i+2} - \xi_{n_i}} N_{n_i,1}(\xi) \tag{3.2}$$

$$N_{n_i,2}(\xi) = \frac{\xi - \xi_{n_i}}{\xi_{n_i+2} - \xi_{n_i}} N_{n_i,1}(\xi) + \frac{\xi_{n_i+3} - \xi}{\xi_{n_i+3} - \xi_{n_i+1}} N_{n_i+1,1}(\xi) \tag{3.3}$$

Note that the first term of (3.1) and the second term of the (3.3) are zeros since $N_{n_i-2,1} = N_{n_i+1,1} = 0$. In addition, the term $\frac{N_{n_i-2,1}(\xi)}{\xi_{n_i} - \xi_{n_i-2}}$ appeared in the second term in (3.1) and the first term in (3.2), and for the (3.2) and (3.3) same term appeared as well. So, they introduced that

$$\text{left}(j) = \xi - \xi_{n_i+1-j} \qquad \text{right}(j) = \xi_{n_i+j} - \xi \tag{3.4}$$

and simplify the equation (3.1- 3.3) such that

$$\begin{aligned}
N_{n_i-2,2}(\xi) &= \frac{\text{left}(3)}{\text{right}(0) + \text{left}(3)} N_{n_i-2,1}(\xi) + \frac{\text{right}(1)}{\text{right}(1) + \text{left}(2)} N_{n_i-1,1}(\xi) \\
N_{n_i-1,2}(\xi) &= \frac{\text{left}(2)}{\text{right}(1) + \text{left}(2)} N_{n_i-1,1}(\xi) + \frac{\text{right}(2)}{\text{right}(2) + \text{left}(1)} N_{n_i,1}(\xi) \\
N_{n_i,2}(\xi) &= \frac{\text{left}(1)}{\text{right}(2) + \text{left}(1)} N_{n_i,1}(\xi) + \frac{\text{right}(3)}{\text{right}(3) + \text{left}(0)} N_{n_i+1,1}(\xi)
\end{aligned} \tag{3.5}$$

Piegl *et al.* also discuss the efficient algorithm to compute the derivatives of the B-spline function in [27]. They introduced two-dimensional array of dimension $(p+1) \times (p+1)$ shown in table 3.1, which stores the basis functions into the upper triangle and the knot differences into the lower triangle. Then, computing the derivatives of B-spline functions

Table 3.1: Two-dimensional array of the B-spline functions and the knot differences with polynomial order $p = 2$ (adapted from [27])

$N_{n_i,1}(\xi)$	$N_{n_i-1,1}(\xi)$	$N_{n_i-2,2}(\xi)$
$\xi_{n_i+1} - \xi_{n_i}$	$N_{n_i,1}(\xi)$	$N_{n_i-1,2}(\xi)$
$\xi_{n_i+1} - \xi_{n_i-1}$	$\xi_{n_i+2} - \xi_{n_i}$	$N_{n_i,2}(\xi)$

(2.27) by the knot differences in two-dimensional array (table 3.1), the coefficients $a_{k,j}$ (2.28) may be found out. For the sake of the convenience, let's call the definition that compute the

B-spline functions $N = [N_{ni-p,p}, N_{ni-p+1,p}, ..., N_{ni,p}]$ and the corresponding first derivatives $dNdxi$ Bspline_basis_and_deriv such that

$$[N, dNdxi] = \text{Bspline\_basis\_and\_deriv}[p, \Xi, ni, \xi] \tag{3.6}$$

where p: polynomial order of the B-spline functions, Xi: knot vector, ni: NURBS coordinate, and ξ: evaluation point, respectively. The algorithm and examples for both the B-spline functions and the derivatives can be found as Algorithm 2.3 in [27].

Once the B-spline functions and the derivatives are found, NURBS basis functions R and the derivative with repect to the parameter space $dRdxi$ can be computed and they are denoted by NURBS_derivatives such that

$$\begin{aligned}[R, dRdxi] = \text{NURBS\_derivatives}[p, q, N, M, dNdxi, dMdeta, ... \\ scatter, P, Number\_nodes\_element]\end{aligned} \tag{3.7}$$

where p, q: orders of the polynomials in ξ- and η-directions, N, M: B-splines functions in ξ- and η-directions, $dNdxi, dMdeta$: the drivatives with respect to ξ- and η-directions, $scatter$: global indices of nodes/control variables, P: control points, and $Number\_nodes\_elements$: number of nodes per element, respectively. Then, the efficient algorithm will be discussed next.

Observing the formulas for the NURBS basis functions (2.33) and the derivatives (2.35), it is necessary to compute the tensor product of B-spline functions and the corresponding weights such that

$$W(\boldsymbol{\xi}) = \sum_{i=1}^{n} R_i^p(\boldsymbol{\xi})\omega_i \tag{3.8}$$

and the tensor product of the derivatives and the corresponding weights with respect to the parameter space ξ or η each such that

$$W'(\boldsymbol{\xi}) = \sum_{\hat{i}=1}^{n} N'_{\hat{i},p}(\boldsymbol{\xi})\omega_{\hat{i}}. \tag{3.9}$$

Then, these enable to use the formula (2.33) and (2.35) to compute the NURBS basis functions and the derivatives with respect to parameter space. The algorithm 1 shows the routine

for the NURBS basis functions and the derivatives at the NURBS coordinates ni(ξ-direction) and nj(η-direction), respectively.

Algorithm 1: NURBS_derivatives(adapted from [18])

Input: p, q, Ξ, H, ni, nj ,N, M, dNdxi, dMdeta, scatter, P, Number_nodes_element

Output: NURBS basis functions R and the derivatives dRdxi with respect to ξ and η, respectively.

[N,dNdxi] = Bspline_basis_and_deriv(p,Ξ,ni,ξ)

[M,dNdeta] = Bspline_basis_and_deriv(q,H,nj,η)

Initialization

for *j in range(0,q+1)* **do**

  for *i in range(0,p+1)* **do**

    # Compute numerator of NURBS basis functions R by (2.46)

    # Compute W($\boldsymbol{\xi}$) by (3.8)

    # Compute W'(ξ) by (3.9)

    # Compute W'(η) by (3.9)

  end

end

for *local_number in range(1,Number_nodes_element+1)* **do**

  # Compute NURBS basis functions R by (2.33)

  # Compute the derivatives wrt. ξ: dRdxi by (2.35)

  # Compute the derivatives wrt. η: dRdxi by (2.35)

end

3.1.2 Element Routine

In the process of the assemble routine in both IGA and FEM, it is very important to track the nodal/control variables both locally and globally. In addition, when evaluating the NURBS

basis functions, it is also important to understand which control variables are corresponding to the NURBS basis functions. Thus, two arrays proposed in [18] should be introduced, that are IEN array also called Element Connectivity array, and INC array called also NURBS Coordinate array as well.

Once the geometry is decided, and refinement is implemented, construction of the NURBS coordinate array is needed in order to find the corresponding knots' indices of knot spans, and that is a function that returns the NURBS coordinate in global sense such that

$$\begin{aligned} n_i &= \text{NURBS\_coordinate}[A, 1] \\ n_j &= \text{NURBS\_coordinate}[A, 2] \end{aligned} \tag{3.10}$$

where A is a global basis function number or node number. The row number of the NURBS_coordinate represents the nodal/control variable number, and the column number represents the directions of the NURBS coordinate, ξ and η.

In addition to that, it is also required to define the element. Knowing each element node numbers gives a simple way to compute the NURBS basis functions using the algorithm 1. Defining the element e whose local basis function number is b, then Element_connectivity array can be defined as

$$B = \text{Element\_connectivity}[e, b] \tag{3.11}$$

where B is the corresponding global basis function number. The algorithm 2 shows the algorithm to create the NURBS coordinate array and the Element connectivity array. Deep explanation can be found in [18].

3.1.3 IGA Implementation Framework

IGA implementation using NURBS basis functions is very similar to FEA implementation framework. One of the main difference between them is the routine for basis function which is shown above as algorithm1 using Python environment. Another major difference is to construct the NURBS coordinate array to store the knot spans' information, meaning that it is required to track the indices of knots when evaluating NURBS basis function. Therefore,

Algorithm 2: Element_Nodes_connectivity(adapted from [18])

```
Input: Number_cp_xi, Number_cp_eta, p, q, element_number
Output: NURBS coordinate array and the Element connectivity array
# Pre-calculations
Number_elements = (Number_cp_xi-p)*(Number_cp_eta-q)
Number_nodes = Number_cp_xi*Number_cp_eta
Number_nodes_element = (p+1)*(q+1)
for j in range(1,Number_cp_eta+1) do
    for i in range(1,Number_cp_xi+1) do
        A = A + 1 # Global function number
        NURBS_coordinates[A-1,0] = i
        NURBS_coordinates[A-1,1] = j
        if j ≥ q+1 then
            if i ≥ p+1 then
                e = e + 1 # Elmenet number
                for jloc in range(0,q+1) do
                    for iloc in range(0,p+1) do
                        # Compute global basis function number B
                        B = A - jloc*Number_cp_xi - iloc
                        # Compute local basis function number b
                        b = jloc*(p+1) + iloc + 1
                        Element_connectivity[e-1,b-1] = B
                    end
                end
            end
        end
    end
end
```

the main difference in NURBS-based IGA is about assembling routine that construct the global stiffness matrix using the two notations mentioned above in section 3.1.1 and 3.1.2.

Assembling

The concept of assembling in NURBS-based IGA is the same as the one in a classical FEM and introduced in section 2.3.3, but it is necessary to modify the basis function routine and element routine. The basic concept of assembling is the same as the one in a classical FEM, which means that it is required to crate two loops to assemble the system, the one of them is looping through every single elements to compute each element stiffness matrix, and the another one is looping over Gauss quadrature points to evaluate the elasticity matrix each integration point.

In assembling routine, first decide element connectivity **scatter** and the NURBS coordinates n_i and n_j for a certain element e using the subroutines shown in algorithm 2. The **scatter** is the element connectivity array which specifies an element e using the global basis function number, and it doesn't only account on the connectivity between local basis function number and global basis function numbers (x-component of the control variables), but also it accounts on y-component of the control variables such that

$$\begin{aligned} \mathbf{scatter\_xy}[\mathbf{0}, \mathbf{0} :: \mathbf{2}] &= 2 * \mathbf{scatter} - 1 \\ \mathbf{scatter\_xy}[\mathbf{0}, \mathbf{1} :: \mathbf{2}] &= 2 * \mathbf{scatter} \end{aligned} \tag{3.12}$$

Once the element connectivity array and the NURBS coordinates are computed, the element stiffness matrix can be computed following the routine bellow:

1. Inside the Gauss quadrature loop, map the quadrature points $\tilde{\xi}$ and $\tilde{\eta}$ into parameter domain, denoted by ξ and η using (2.60) and the NURBS coordinates n_i and n_j.

2. Compute the determinant of the Jacobian between parameter space and parent space $J_{\tilde{\boldsymbol{\xi}}}$ using (2.62) and NURBS basis functions and the derivatives with respect to parameter domain $[\mathbf{R}, \mathbf{R}_\xi]$ by the function introduced above (3.7) or algorithm 1.

3. Compute the determinant of the Jacobian between parameter space and physical space $J_{\boldsymbol{\xi}}$ using (2.65) and (2.66).

4. Compute the derivatives of the NURBS basis functions with respect to physical coordinate $\mathbf{R}_{,\mathbf{x}}$ to form the strain-displacement matrix $\mathbf{B}$ by (2.67) and (2.66).

5. Compute the element stiffness matrix $\mathbf{K}^e$ by (2.74).

Then it is possible to loop this routine above through the every single element in order to construct the global stiffness matrix. The assembling routine algorithm is shown in algorithm 3 for Python environment. Any other routines for IGA are very similar to a classical FEM algorithm and can be cited in [19].

3.2 Isogeometric Analysis in MATLAB Environment

NURBS-based Isogeometric Analysis has been implemented using the MATLAB environment in [24]. Thanks to their work in [24], a linear elasticity two-dimensional problem on isotropic materials can be implemented and the visualization has also been enabled by MATLAB and Paraview. This MATLAB IGA code can also implement refinement using knot insertion described in section 2.3.2. The code architecture of this IGA MATLAB is almost the same as the ones coded in Python environment described above in section 3.1, however, this computes the NURBS basis functions and the derivatives via C language for the sake of efficiency and then return them in MATLAB format.

In this research, a two-dimensional linear elasticity problem assuming isotropic material under plane-stress condition has been implemented first, then the IGA MATLAB code is modified to analyze on the composites reinforced by curvilinear fibers under the same assumption except CTI materials. In order to save memory usage and time consumption, the subroutines for the assembling part and the element stiffness computation part discussed in section 3.1 are rewritten using the concept of parallelization and vectorization.

Algorithm 3: Global Element Stiffness Matrix Assemble (adapted from [24])

Output: Global stiffness matrix $\mathbf{K}$

\# Loop over elements/knot spans

for *e in range(1,nel+1)* **do**

- \# Initialize for $\mathbf{B} = 0$ and $\mathbf{K^e} = 0$
- \# Get element connectivity (3.11): **scatter** = Element_connectiviy[e-1,:]
- \# Compute the connectivity array for $\mathbf{B}$: **scatter_xy** by (3.12)
- \# Get NURBS coordinate (3.10):
- ni = NURBS_coordinate[**scatter**[0,0]-1,0]
- nj = NURBS_coordinate[**scatter**[0,0]-1,1]
- **for** *gp in range(1,numbrt_gps+1)* **do**
  - \# Get the Gauss points and the weight: $\tilde{\boldsymbol{\xi}}$ and W_{gp}, respectively
  - \# Compute $\boldsymbol{\xi}$ at the NURRBS coordinates ni and nj by (2.60)
  - \# Compute the Jacobian $J_{\tilde{\boldsymbol{\xi}}}$ by (2.62)
  - \# Compute the NURBS basis and the derivative w.r.t. parameter space by $[\mathbf{R}, \mathbf{R}_{,\xi}] =$ NURBS_derivatives[p,q,N,M,dNdxi,dMdeta,scatter,P,Number_nodes_element] (3.7) using control points $\mathbf{P}[\mathbf{scatter} - 1, :]$
  - \# Compute the Jacobian $J_{\boldsymbol{\xi}}$ by (2.65) and (2.66)
  - \# Compute the spatial derivatives of the NURBS $\mathbf{R}_{,\mathbf{x}}$ basis by (2.67)
  - \# Compute the strain-displacement matrix $\mathbf{B}$ by (2.68)
  - \# Compute the lcoal stiffness matrix $\mathbf{K}^e$ by (2.74) s.t. $\mathbf{K}^e = \mathbf{B}.T * \mathbf{D} * \mathbf{B} * J_{\tilde{\boldsymbol{\xi}}} * J_{\boldsymbol{\xi}} * W_{gp}$
- **end**
- \# Compute the global stiffness matrix s.t. $\mathbf{K}[\mathbf{scatter\_xy} - 1, \mathbf{scatter\_xy}.T - 1] = \mathbf{K}[\mathbf{scatter\_xy} - 1, \mathbf{scatter\_xy}.T - 1] + \mathbf{K}^e$

end

3.3 Isogeometric Analysis on Semi-circular Hole Plate of Isotropic Material

Isogeometric Analysis has been implemented using the IGA MATLAB [24] on a semi-circular hole plate assuming a linear elastic isotropic problem illustrated in figure 3.1 under the following conditions

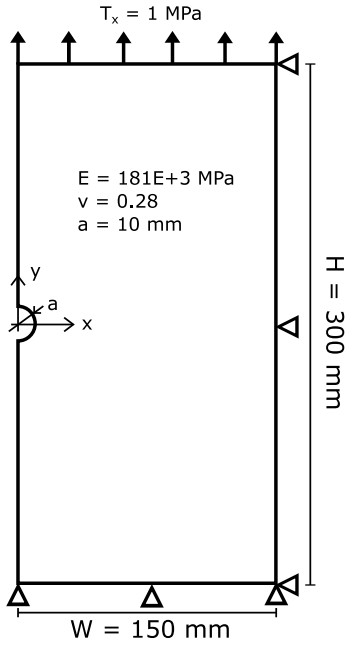

Figure 3.1: Elastic plate with a semi-circular hole: Problem set-up

1. The 150×300 mm^2 plate has a semi-circular hole with a radius $a = 10$ mm at the middle of the left edge and assumed as plane-stress condition with a unit thickness.

2. The plate is undergoing the traction in the positive y-direction as $T_y = 1$ MPa in physical coordinate.

3. The plate of the bottom edge is constrained in y-direction and the right edge is constrained in x-direction.

4. The material can be defined by these engineering properties, Young's modulus E as 181×10^3 MPa and Poisson's ratio ν as 0.28

5. The geometry can be defined by the following knot vectors

$$\Xi = [0, 0, 0, 0.25, 0.5, 0.5, 0.75, 1, 1, 1] \tag{3.13}$$

$$H = [0, 0, 0, 1, 1, 1] \tag{3.14}$$

with the polynomial order $p = 2$ and $q = 2$, and the corresponding control points and weights are summarized in table 3.2. The Gaussian quadrature rule has been used for the evaluation, and decided to use 4×4 integration points.

Using the knot vectors Ξ and H defined in (3.13) and (3.14), it is possible to construct the exact geometry of our modeling object shown in figure 3.2a, and figure 3.2b shows the refined elastic plate by knot insertion explained in section 2.3.2. The circumferential clockwise direction is defined as positive ξ-direction and radial direction as positive η-direction in parameter domain, so that the corresponding control points and the weights are assigned by the orientation rule. The mesh refinement has been implemented by the concept of the knot insertion discussed in section 2.3.2, and refinement 5 in figure 3.2b means that refinement (knot insertion) has been implemented five times, uniformly for the sake of simple comparison between two different numerical methods.

3.3.1 Convergence Rate of IGA

Figure 3.3 shows the contour plots of the y-component of the stress σ_{yy} with several refinements. As can be noted, the higher refinement we have, the contour plots of the stress field have smoother contour. They has C^1-continuity at the element boundary except x-axis. A repeated control point can be possible at the top-right and bottom-right corner of the plate, and it causes a singularity when implementing the inverse of Jacobian matrix (2.65). The singularity does not cause any issue in this analysis, however, it is not appropriate to evaluate

Table 3.2: Control Points for a semi-circular hole notched plate without any refinements

i	j	$P_{i,j}$	$\omega_{i,j}$
1	1	(0,10)	1
2	1	(4.1421,10)	0.8536
3	1	(10,4.1421)	0.8536
4	1	(10,0)	1
5	1	(10,-4.1421)	0.8536
6	1	(-4.1421,-10)	0.8536
7	1	(0,-10)	1
1	2	(0,80)	1
2	2	(28.9949,80)	1
3	2	(80,28.9949)	1
4	2	(80,0)	1
5	2	(80,-28.9949)	1
6	2	(-28.9949,-80)	1
7	2	(0,-80)	1
1	3	(0,150)	1
2	3	(150,150)	1
3	3	(150,150)	1
4	3	(150,0)	1
5	3	(150,-150)	1
6	3	(150,-150)	1
7	3	(0,-150)	1

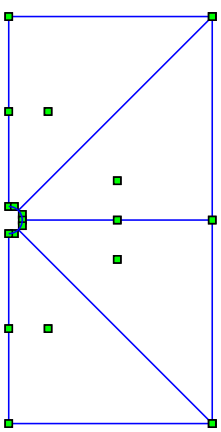

(a) Initial mesh and the control points

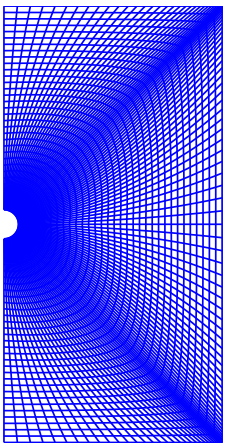

(b) Refinement 5

Figure 3.2: (a) Initial mesh with control points of elastic plate with a semi-circular hole. (b) Mesh refinement implemented by knot insertion.

the integrated at the point of singularity [4]. Although our geometry has singularity, IGA still works properly and robustly.

In order to compare these two numerical method, let's define the following to properties: (1) the maximum diagonal length of the elements h_{max} found in the mesh and (2) the error in percentage from the converged value such that

$$\text{Error} = |K_t^{\infty} - K_t|/K_t^{\infty} * 100 \tag{3.15}$$

where K_t^{∞} represents the converged stress concentration factor. The stress concentration factor K_t is defined by

$$K_t = \sigma_{yy}^{max}/\sigma_{applied} \tag{3.16}$$

where σ_{yy} is the maximum stress of the y-component found in the plate, and $\sigma_{applied}$ is the applied stress on the top edge, that is 1 MPa in this case. The FEM implementation has been done using the MATLAB FEM code built on my own. The basis function was

chosen as bi-linear Lagrange polynomials and quadrilateral rectangular element was used for this simulation. Since refinement(knot insertion) is implemented uniformly in IGA, the refinement of FE model is also implemented uniformly in order to compare two different numerical method using the maximum diameter h_{max} of the mesh found in the element.

Figure 3.4 shows plots of the percentage error (3.15) against the maximum diagonal length h_{max} found in the mesh. As can be noted in the figure, blue line represents the result from IGA and the red one is from FEM. There are two regions with two different convergence rates in both FEM and IGA. First region where mesh size is relatively coarse has much slower rate. Once mesh size becomes smaller than certain value, both numerical methods transit to the faster converging region. Although the two rates of convergence for both FEM: 2.14 and IGA: 2.04 are very close each, the IGA experiences convergence much faster than FEM because percentage error in IGA is overlay smaller than the one in FEM. The rate of convergence for quadratic NURBS basis functions is about 2 in IGA.

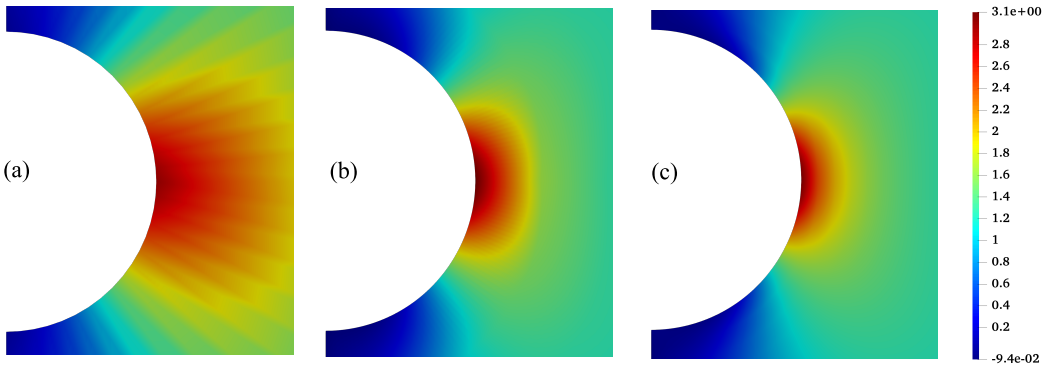

Figure 3.3: Contour plots of stress in y-direction σ_{yy} from quadratic NURBS basis function with (a) refinement 3, (b) refinement 5, (c) refinement 7. The stress concentration factor K_t is around 3.1.

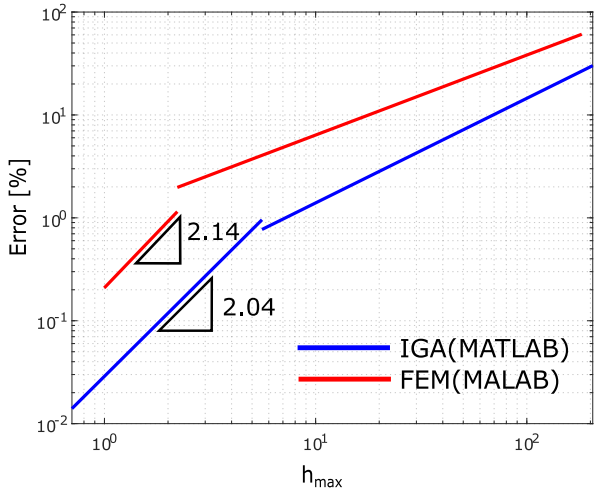

Figure 3.4: Error comparison between IGA and FEM: isotropic case. The both x- and y-axis are logarithmed.

3.4 Parallelization and Vectorization

It is possible to optimize the computational cost and the time-consumption reducing the size of global stiffness matrix by a usage of local refinement around a semi-circular hole. However, only uniform refinement has been implemented for the sake of simple comparison between FEM and IGA, thus the computational cost is very high. In addition, it might be necessary to refine meshes around the edges of the notched plate on the CTI composites as well because the fibers have a possibility to follow the continuous curvilinear paths around the edges as well. Due to the issues, new routine can be introduced in order to overcome those burdens by the use of parallel computing and vectorization method for the assembling part (algorithm 3).

3.4.1 Parallelization

In fact, the mesh size of the FE model and Isogeometric model have strong impact on the accuracy of the approximation. FE model and Isogeometric model require fine meshes as many as possible which contains a large number of elements to obtain high accuracy of the solution space, therefore it is worth to optimize the element stiffness computation subroutine using parallel computing.

In this paper, the parallel computing for the element stiffness matrix has been implemented by the use of MATLAB Parallel Computing Toolbox built-in function *parfor*. Parallel computing enables to compute each element stiffness matrix simultaneously by assigning each job to multiple workers(CPU cores). The key is that the scripts in the *parfor* has to be independent from previous/future jobs. More solid basics of parallel computing can be found in the document of Parallel Computing Toolbox [1] published by MathWorks.

In order to parallelize the computation routine for element stiffness matrix, a three-dimensional element stiffness array $\mathbf{K}^e$ is defined as

$$\mathbf{K}^e_{noDOFs \times noDOFs \times noElems} = \mathbf{K}^e(:,:,e) + \mathbf{K}_{local} \tag{3.17}$$

where $\mathbf{K}_{local}$ is a element stiffness matrix at element e and $noDOFs$ and $noElems$ are the number of the degree of freedoms and the number of elements, respectively. Thus, the three-dimensional element stiffness matrix $\mathbf{K}^e$ stores all of the element stiffness matrices in the structure. This method enable to compute the element stiffness in parallel, however, it takes a large portion of memory usage to create a large size of the three-dimensional matrix. This large memory usage causes some problem due to the lack of the memory in the general desktop computer. To solve this memory shortage, the supper computer system called Hyak from University of Washington, Seattle has been utilized

3.4.2 Vectorization

Although computing element stiffness in parallel helps to save time consumption and computational expense, it is still required to assemble the global stiffness matrix. In general,

Algorithm 4: Compute_Element_Stiffnesses

Output: Three-dimensional element stiffness matrix array $\mathbf{K}^e$

parfor *e = 1:noElems* **do**

Initialize for $\mathbf{B} = 0$

Compute knot spans: **xiE**, **etaE** (See the refference [24])

Get scatter vector from element connectivity array: **sctr** = element(e,:)

for *gp = 1:noGPs* **do**

Compute Gauss points in parameter space by (2.60): ξ, η

Compute the Jacobian (2.62) by the knot spans: $J_{\tilde{\boldsymbol{\xi}}}$

Compute NURBS derivatives $[\mathbf{R}_{,\xi}\,, \mathbf{R}_{,\eta}\,]$ (See the refference [24])

Compute the Jacobian $J_{\boldsymbol{\xi}}$ by (2.65) and (2.66)

Compute the spatial NURBS derivatives $[\mathbf{R}_{,x}\,, \mathbf{R}_{,y}\,]$ by (2.67)

Construct the strain-displacement matrix $\mathbf{B}$ (2.68)

Compute the local stiffness matrix (2.74):

$\mathbf{K}^e(:,:,e) = \mathbf{K}^e(:,:,e) + \mathbf{B}^T\mathbf{C}\mathbf{B}J_{\tilde{\boldsymbol{\xi}}}J_{\boldsymbol{\xi}}$

end

end

* The array element represents the element connectivity array defined in algorithm 2.

**noELems*, *noGPs*, and *noCtrPts* are the number of elements, the number of Gauss quadrature points, and the number of control points, respectively.

*Note that the detail algorithms except $\mathbf{K}^e$ evaluation part for parallelization can be found in [24].

it takes much longer to implement matrix operation and for-loop than vector operation in MATLAB. Thus, vector operation is utilized without for-loop or matrix operation as much as possible in the assemble routine.

To vectorize the assemble subroutine, it is important to understand the sparse matrix notation. MATLAB supports this notation as one of the built-in functions called *sparse*, denoted by

$$\mathbf{S} = sparse(I, J, K, m, n) \tag{3.18}$$

and returns a sparse matrix $\mathbf{S}$ of the size $m \times n$ such that

$$\mathbf{S}(I(e), J(e)) = K(e) \tag{3.19}$$

where the vectors I, J, and K have the same size, and zero elements are not stored in K.

Define the $n * noELems \times 1$ vectors I_g, J_g, and K_g as

1. K_g contains the elements of all local stiffness matrices $\mathbf{K}^e$ column-wise,

2. I_g contains the global row indices stored in K_g, correspondingly,

3. J_g contains the global column indices stored in K_g, correspondingly,

where n and $noElemes$ are the number of basis functions per element and the number of elements, respectively. Then, applying to the MATLAB built-in sparse matrix (3.18) enables to construct the global stiffness matrix $\mathbf{K}$ such that

$$\mathbf{K} = sparse(I_g(:), J_g(:), K_g(:), noDOFs, noDOFs), \tag{3.20}$$

and the the algorithm is shown in algorithm 5.

Figure 3.5 shows the time-consumption against the number of degree of freedom for both (1): the classical method (algorithm 3) and (2): the optimized method (algorithm 4 and 5), which is modified by the use of parallel computing and vectorization explained above section 3.4.1 and 3.4.2. As can be seen in the figure, the optimized method is slightly slower than

Algorithm 5: Assemble_Global_Stiffness

Assembling routine for two-dimensional nine-node element mesh

Output: Global stiffness matrix **K**

Create I_g and J_g vectors from element connectivity:

i = 1:18

ii = i'*ones(1,18), jj = ii'

me = [element': element' + noCtrPts]

Ig = me(ii(:),:)

Jg = me(jj(:),:)

Construct Global Stiffness Matrix by (3.20):

K = sparse(I_g(:),J_g(:),$\mathbf{K}^e$(:), noDOFs, noDOFs)

* $\mathbf{K}^e$ is computed by algorithm 4.

a classical method in a small-scale structure, however, the optimized method becomes way more faster once the number of degree of freedom meets a certain point. At the very end points, the optimal method reduces the time-consumption to 1.5 minutes, which is about 480 times faster than the classical method (12 hours).

The full discussion of this vectorization is explained in [7] and it also compares to other programming environment like Octave and FreeFEM++.

3.5 Isogeometric Analysis on Semi-circular Hole Plate of Curvilinear Fiber Reinforced Composite Materials

NURBS-based Isogeometric Analysis has been implemented using the MATLAB environment in [24]. In this paper, multiple analysis on composite materials reinforced by curvilinear fibers are implemented assuming a two-dimensional linear elasticity problem under plane-stress condition. Thanks to their work in [24] for an isotropic two-dimensional problem and the visualization enabled by MATLAB environment and Paraview, IGA implementation frame-

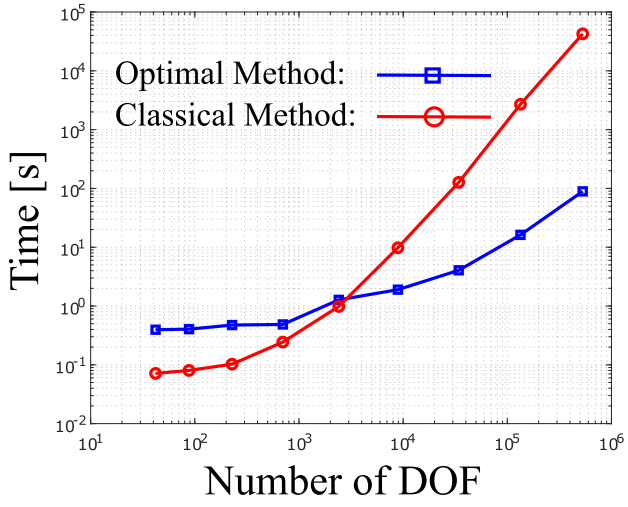

Figure 3.5: Time-consumption against the number of degree of freedom by the two methods, (1) optimal method and (2) classical method.

work for the composite materials reinforced by curvilinear fiber path can be implemented only modifying the element stiffness assemble routine (algorithm 3).

The implementation framework for CTI materials are basically the same as the one shown in algorithm 3, but the subroutine for the computation of material stiffness which is depend on the fiber orientation θ. Thus, it is required to focus on an computation of the element stiffness routine enabled by parallelization and vectorization in the case of CTI materials.

As mentioned in section 2.3.4, it is widely used to discretize the curvilinear fiber orientation θ as constant each element [15], however, the new evaluation method which enable to capture the curvilinear fiber path more precisely is proposed updating fiber orientation θ each integration point but element. Algorithm 6 shows the brief script of IGA MATLAB for CTI materials, and the only difference between the one for Isotropic and CTI is elasticity matrix computation process. It is updating the elasticity matrix each integration point using transformation matrices (2.18) and (2.19) and the formula (2.10). The assembling routine and any other routines are the same as the one for isotropic materials (algorithm 5 for as-

semble routine). The implementation results of analysis on the curvilinear fiber reinforced composites will be discussed and shown in next chapter.

Algorithm 6: Element Stiffness Matrix Computation for CTI Materials

Output: Element Stiffness Array $\mathbf{K}^e$ defined in (3.16)

Loop through elements/knot spans

parfor *e = 1:noElems* **do**

  # Initialize for $\mathbf{B} = 0$

  # Compoute the knot spans and the indices:

  xiE, **etaE**, and **span** = [uspan; vspan] (See the reffrence [24])

  # Get element connectivity array: **sctr** = element(e,:)

  for *gp = 1:noGPs)* **do**

    # Compute Gauss points in parameter space by (2.60): ξ, η

    # Compute the Jacobian (2.62) by the knot spans: $J_{\tilde{\boldsymbol{\xi}}}$

    # Compute NURBS basis and the derivatives $[\mathbf{R}_{,\xi}\,, \mathbf{R}_{,\eta}]$ (See the refference [24])

    # Compute the Jacobian $J_{\boldsymbol{\xi}}$ by (2.65) and (2.66)

    # Compute the spatial NURBS derivatives $[\mathbf{R}_{,x}\,, \mathbf{R}_{,y}]$ by (2.627

    # Construct the strain-displacement matrix $\mathbf{B}$ (2.68)

    # Compute Gauss points in physical space x and y by (2.58)

    # Update the fiber orientation θ by (2.71)

    # Compute the transformation matrix $\mathbf{T}_\sigma$ and $\mathbf{T}_\epsilon$ from (2.17) and (2.18)

    # Compute the elasticity matrix: $\overline{\mathbf{C}} = \mathbf{T}'_\sigma * \mathbf{C} * \mathbf{T}_\epsilon$

    # Compute the local stiffness matrix (2.74):

    $\mathbf{K}^e(:,:,e) = \mathbf{K}^e(:,:,e) + \mathbf{B}^T\overline{\mathbf{C}}\mathbf{B}J_{\tilde{\boldsymbol{\xi}}}J_{\boldsymbol{\xi}}$

  end

end

Chapter 4
MECHANICAL POINT OF VIEWS

The NURBS-based Isogeometric Analysis has been discussed theoretically in chapter 3 and the implementation is introduced in chapter 3. In this thesis, the NURBS-based Isogeometric Analysis and classical FEM have been implemented on the curvilinear transverse isotropy material (CTI), and discussed on comparison between IGA and a conventional FEA on the numerical performance and the mechanical behaviors of the CTI composites. In addition to that, single variable optimizations are conducted for two objective variables: (1) stress concentration factor and (2) Tsai-Wu index.

4.1 Analysis on the Composites Reinforced by Curvilinear Fibers

Multiple simulations enabled by IGA has been implemented on the plate featuring the CTI weakened by semi-circular hole notch shown in figure 4.1 under the following conditions:

1. The 150×300 mm^2 is weakened by a semi-circular hole with a radius $a = 10$ mm at the middle of the left-hand edge and assumed as plane-stress condition with a unit thickness.

2. The plate is undergoing the traction in the positive y-direction as $T_y = 1$ MPa in physical coordinate.

3. The plate of the bottom edge is constrained in y-direction and the right-hand edge is constrained in x-direction.

4. For the FEM simulations the basis function was chosen as bi-linear Lagrange polynomial, which means quadrilateral rectangular element type has been applied.

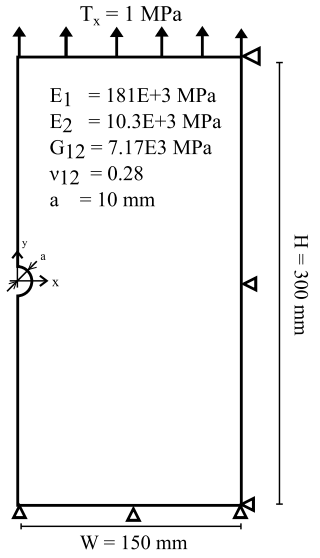

Figure 4.1: Elastic Plate featuring curvilinear transverse isotropy weakened by a 10 mm semi-circular notch.

5. The material system used in the simulations are characterized with following properties: Young's modulus in the x_1 direction E_1 as 181×10^3 MPa, Young's modulus in the x_2 direction E_2 as 10.3×10^3 MPa, shear modulus in the $x_1 - x_2$ plane G_{12} as 7.17×10^3 MPa, and Poisson's ratio in the $x_1 - x_2$ plane ν_{12} as 0.28.

6. The geometry is defined by the following knot vectors

$$\Xi = [0, 0, 0, 0.25, 0.5, 0.5, 0.75, 1, 1, 1] \tag{4.1}$$

$$H = [0, 0, 0, 1, 1, 1] \tag{4.2}$$

with the polynomial order $p = 2$ and $q = 2$, and the corresponding control points and weights are summarized in table 3.2.

7. The Gaussian quadrature rule has been used for the evaluation, and decided to use 4×4 integration points.

8. The ply strengths: (1) σ_{1t}^f, σ_{1c}^f are tensile and compression strengths in the fiber direction, (2) σ_{2t}^f, σ_{2c}^f are tensile and compression strengths perpendicular to the fibers, (3) τ_{12}^f is shear strength are assigned and tabulated in table 4.1.

Table 4.1: Table of ply strengths in MPa.

σ_{1t}^f	σ_{1c}^f	σ_{2t}^f	σ_{2c}^f	τ_{12}^f
1500	1500	40	246	68

Multiple simulations have been implemented using both MATLAB IGA and a classical FEM (built on my own) on the following CTI materials: (1) Curvilinear fiber path following semi-circular notch (figure 4.2a), (2) Concentric fiber paths covering semi-circular notch (figure 4.2b), and (3) longitudinal and transverse straight fibers (figure 4.2c and 4.2d). Since

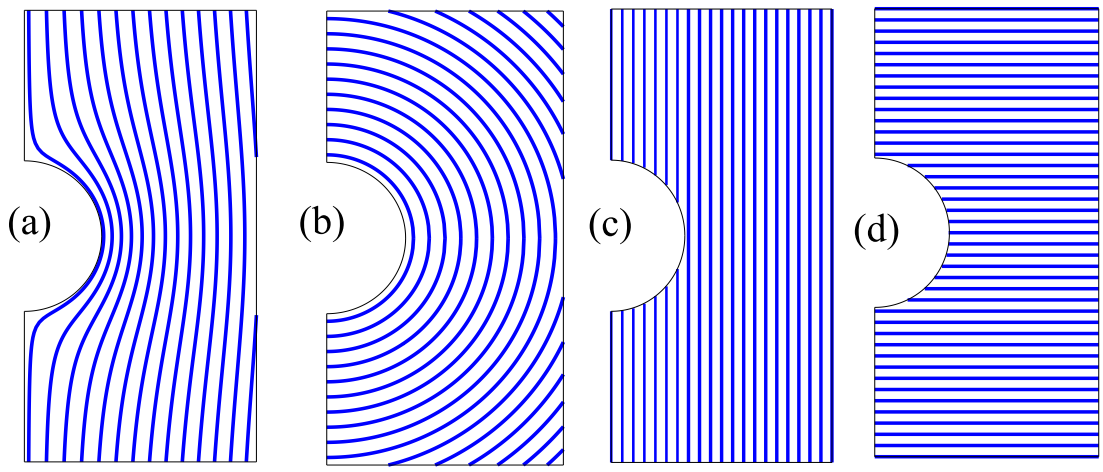

Figure 4.2: Composites reinforced by curvilinear fibers: (a) Curvilinear fiber paths following semi-circular notch, (b) Concentric fiber paths, (c) longitudinal straight fiber paths, (d) transverse straight fiber paths.

this MATLAB IGA solver has limitation in a local refinement by the use of knot insertion, an

uniform mesh refinement has been adopted. To compare to each CTI material's mechanical behavior, three following properties are calculated and summarized on table 4.2:

1. The stress concentration factor K_t defined by (3.16).

2. The average stiffness along the top edge $\bar{K}$ such that

$$\bar{K} = \frac{P_{tot}}{\bar{v}} \tag{4.3}$$

where

$$P_{tot} = \int_0^L \sigma_{yy} d\,x \qquad \text{L: Width of the plate,} \tag{4.4}$$

and

$$\bar{v} = \frac{1}{L}\int_0^L v d\,x. \tag{4.5}$$

where σ_{yy} and v are the longitudinal stress and displacement along the top edge, respectively.

3. Tsai-Wu failure index Φ assuming transverse isotropy under plane-stress condition such that

$$\Phi = F_1\sigma_1 + F_2\sigma_2 + F_{11}\sigma_1^2 + F_{22}\sigma_2^2 + F_{66}\tau_{12}^2 + 2F_{12}\sigma_1\sigma_2 \tag{4.6}$$

where

$$\begin{aligned} F_1 &= \frac{1}{\sigma_{1t}^f} - \frac{1}{\sigma_{1c}^f}, \qquad & F_{11} &= \frac{1}{\sigma_{1t}^f\sigma_{1c}^f} \\ F_2 &= \frac{1}{\sigma_{2t}^f} - \frac{1}{\sigma_{2c}^f}, \qquad & F_{22} &= \frac{1}{\sigma_{2t}^f\sigma_{2c}^f} \\ F_{66} &= \frac{1}{\tau_{12}^f}, & & \\ F_{12} &= -\frac{1}{2}\sqrt{F_{11}F_{22}}. & & \end{aligned} \tag{4.7}$$

and σ_{ij} is computed from transforming the stress in global coordinate into the local coordinate using the transformation matrix (2.32).

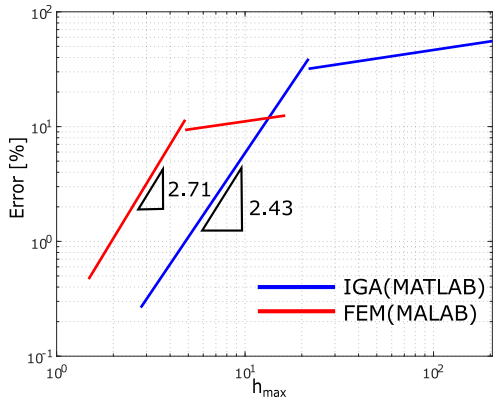

(a) Curvilinear fiber paths following semi-circular notch

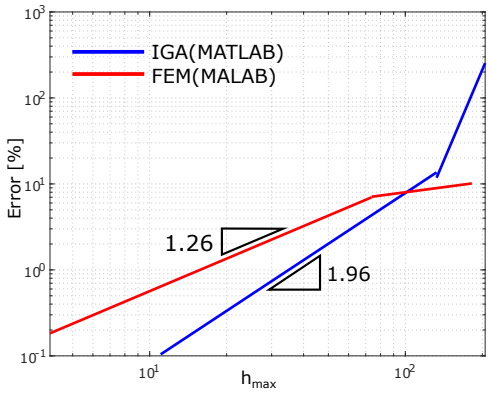

(b) Concentric fiber paths

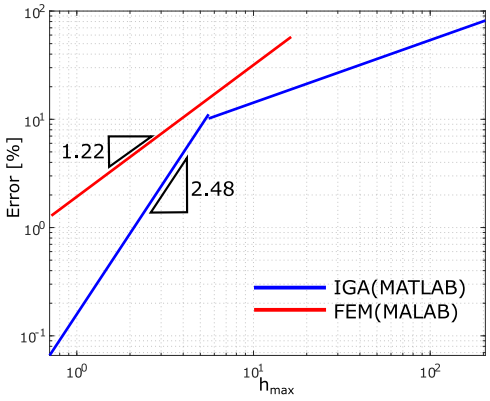

(c) Longitudinal straight fiber path.

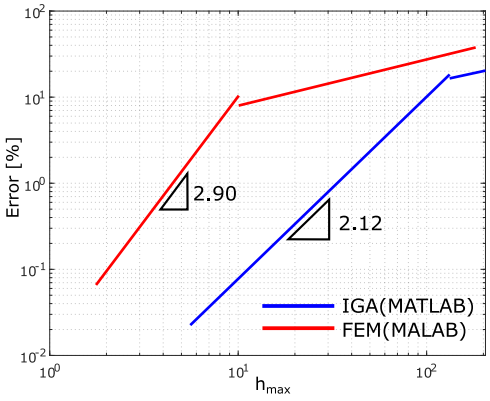

(d) Transverse straight fiber path.

Figure 4.3: Error comparisons between IGA and FEM of four different CTI composites. The both x- and y-axis are logarithmed.

4.1.1 Curvilinear Fiber Paths Following Semi-circular Notch

Curvilinear Transverse Isotropy(CTI) materials are not only attracted on the mechanical engineering study, but they are also fascinated in electrostatic study as well. The optimal curvilinear fiber paths (See figure 4.2a) for a minimum electrical residence are derived from closed-form analytically by Salviato *et al.,* in [28]. It is also interesting that the curvilinear fiber paths can be applied in the stress analysis in order to reduce the stress concentration around a semi-circular hole. The fiber orientation as a function of x and y can be calculated using the optimal fiber paths of minimum electrical resistance derived in [28] such that

$$\theta(x,y) = \tan^{-1}\left[\frac{1+\frac{a^2}{x^2+y^2}\cos\left(2\tan\frac{y}{x}\right)}{-\frac{a^2}{x^2+y^2}\sin\left(2\tan\frac{y}{x}\right)}\right] \tag{4.8}$$

where a is a radius of the semi-circular hole. The fiber paths are shown in figure 4.2a.

Rate of convergence

Figure 4.3a represents the error defined in (3.15) as varying the mesh size measured by the concept provided in section 3.1.1, which is the maximum diagonal length h_{max} found in the meshes. For this fiber configuration, FEM initially start with the lower value of percentage error. As can be noted in the figure 4.3a, there are two regions with different convergence rate. First region where the mesh size is relatively coarse has much slower rate. Once the mesh size is smaller than certain value both analysis methods transit to the faster converging region. Although the convergence rate of IGA: 2.43 in this region is slightly slower than the one of FEM: 2.71, percentage error for each element size is still lower in IGA comparing to the FEM in the second region due to the earlier transitioning points.

Mechanical Behavior of the Materials

Figure 4.4 shows the stress fields of x-, y-, and shear components, respectively, from left-hand to right-hand. These contour plots looks similar to traditional traditional longitudinal straight fiber composites (figure 4.6), however, the stress concentration factor K_t is 3.49

(table 4.2) located at a midpoint of the semi-circular notch, which is approximately twice smaller than the one 7.18 of longitudinal straight fiber ply. At the same time, the stiffness $\bar{K}$ for the curvilinear fiber ply and the longitudinal straight fiber ply are similar each other and they are 86.7 GN/mm and 88.2 GN/mm, respectively (table 4.2). These fact implies that although the stiffness is almost the same in both these two materials, the stress σ_{yy} is much less concentrated around a semi-circular hole than the longitudinal straight fiber material. This curvilinear fiber paths reduces the stress concentration, but in a same time the stiffness is still maintained high-value as $\bar{K} = 86.7$ GN/mm.

It is very interesting that even though the stiffness is highly close to each on the top edge in both two materials mentioned above, the stress concentration of the curvilinear fiber reduces much more than the longitudinal straight fiber. The curvilinear fibers around the semi-circular notch have higher curvatures rather than the other region, meaning that the curvilienar fibers are more close to transverse direction rather than the other region. This fiber curvature makes the region more compliant than the other region. This results in the reduction of the stress concentration around the semi-circular notch.

Considering the maximum Tsai-Wu failure index, the maximum Tsai-Wu for the curvilinear fibers following the semi-circular notch is about 0.026, which is much smaller than the ones (table 4.2) from other fiber paths shown in figure 4.2b and figure 4.2d. However, the maximum Tsai-Wu failure index for the longitudinal straight fiber is way more smaller, approximately six times smaller, but the stress concentration is significantly high. Thus, it motivates to design the curvilinear path to have a balanced structure with high stiffness and low concentration factor that will increase the tolerance in damage initiation.

4.1.2 Concentric Fiber Path

In the case of longitudinal straight fiber reinforced composites, the material could have the high-level of stiffness. However, the stress in y-direction is significantly concentrated around the semi-circular hole notch (See figure 4.6b). In order to reduce the stress concentration around the semi-circular hole, the concentric fiber path shown in figure 4.2b is the one of

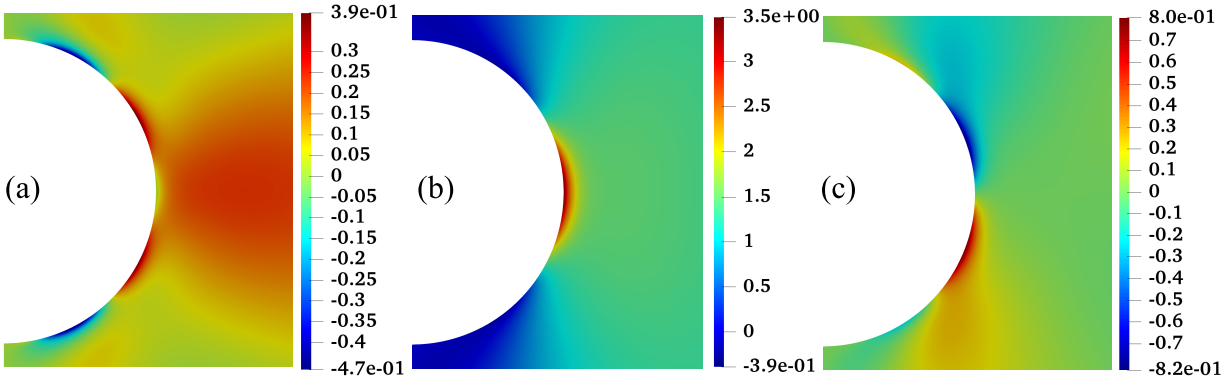

Figure 4.4: Stress fields of composites reinforced by curvilinear fibers following semi-circular notch: (a) Stress in x-direction σ_{xx}, (b) Stress in y-direction σ_{yy}, (c) Shear stress in $x-y$ plane τ_{xy}.

the options having the high rate of curvature around the semi-circular hole.

The concentric fiber path following semi-circular notch is illustrated in figure 4.2b and it is defined by the following function such that

$$\theta(x,y) = \frac{\pi}{2} + \cos^{-1}\frac{x}{R}, \qquad R = \sqrt{x^2+y^2} \tag{4.9}$$

which provide us the fiber orientation at an arbitrary point x and y.

Rate of convergence

Figure 4.3b represents the error plots of IGA and FEM, and the rate of convergences for IGA and FEM are 1.96 and 1.26, respectively. It is obvious that the IGA has higher rate of convergence and converges much faster than FEM. Although IGA starts with the much higher percentage error, its initial convergence rate is very steep so that it reaches the transitioning point very early, eventually out performing FEM.

Mechanical Behavior of the Materials

Figure 4.5 shows the contour plots of stress filed of x-, y-, and shear in $x-y$ plane components from left-hand to right-hand in order for the concentric curved fiber reinforced composites shown in figure 4.2b. Based on table 4.2, the stress concentration factor is about 5.02, and it is located at the middle of the right edge of the plate, but halfway of the semi-circular arc. The stress around semi-circular hole is still concentrated and the stress concentration factor K_t around the notch is roughly 4. According to the stress contour plots for all the components (figure 4.5a,b,c), all the components of stresses are concentrated around the right-hand edge following curviliner concentric fiber paths. The curvilinear fibers close to the semi-circular hole have higher rates of curvatures, which means the fiber orientations are more close to ninety-degree rather than the other region. This implies that the region around the semi-circular hole notch is more compliant. However, the region far away from the semi-circular hole has more close to longitudinal fiber orientations and this results in making the region more stiffer. These two fact tells us that all the components of the stresses are concentrated on the middle of the right-hand edge.

4.1.3 Straight Fiber Paths

The straight fibers for both transverse and longitudinal fiber orientations are also implemented by IGA and FEM to compare these results to the other fiber paths introduced above (See figure 4.2). Figure 4.2c and 4.2d show the straight fiber paths longitudinal to the traction applied and transverse to the applied traction, respectively.

Rate of convergence

As can be noted in the plot of the error for the longitudinal straight fibers reinforced composites (figure 4.3c), the convergence rate of IGA 2.48 is much higher than the one 1.22 by FEM, which implies the IGA is significantly stable rather than FEM in this fiber path. Furthermore, based on figure 4.3d in the case of transverse straight fiber path, the rates

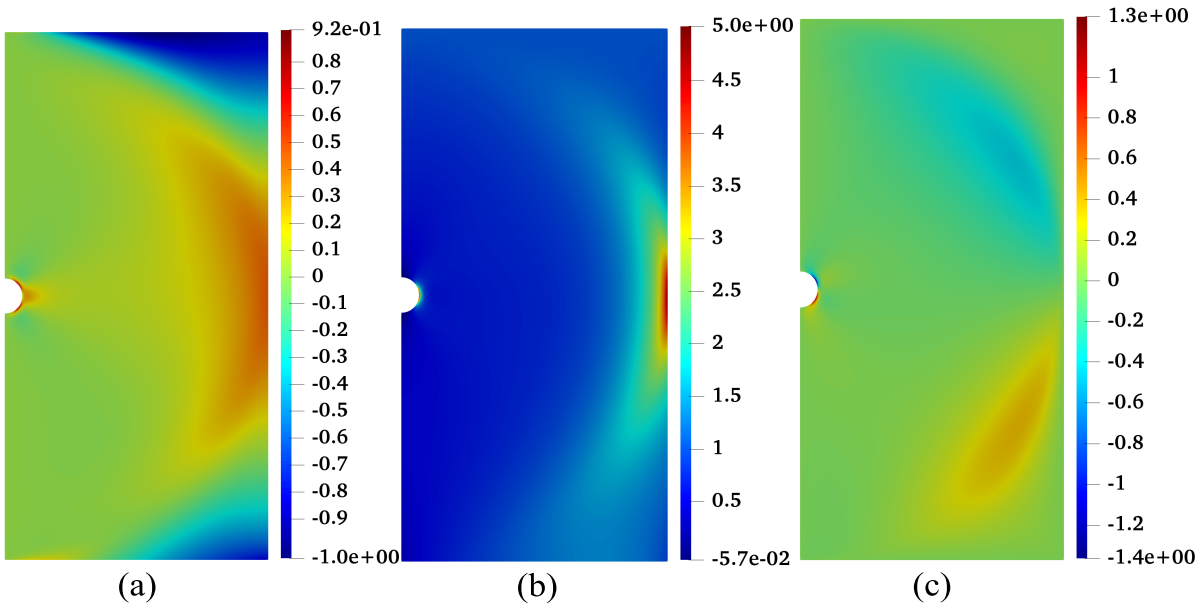

Figure 4.5: Stress fields of composites reinforced by concentric fibers following semi-circular notch: (a) Stress in x-direction σ_{xx}, (b) Stress in y-direction σ_{yy}, (c) Shear stress in $x-y$ plane τ_{xy}.

of convergence are 2.90 and 2.12 for FEM and IGA, respectively, however, again, the IGA still remain the rate of convergence as the mesh size is getting larger and larger like other fiber paths except the longitudinal straight fiber path, but FEM. These concludes that IGA enable to go through a simulation with coarser mesh than the one by FEM.

Mechanical Behavior of the Materials

According to the figure 4.6 and 4.7 for the longitudinal and the transverse straight fiber paths, respectively, the stress concentration and the stiffness along the top edge is under our consideration. Comparing to the curvilinear fiber ply following the semi-circular notch, although the longitudinal straight fiber composite has about twice higher stress concentration, the maximum Tsai-Wu is around six times smaller than the one by curvilinear fiber composites. It is very attractive to obtain very small Tsai-Wu index, however, the stress concentration around the semi-circular notch is significantly high, so that it is better to obtain small stress concentration and Tsai-Wu index at the same time.

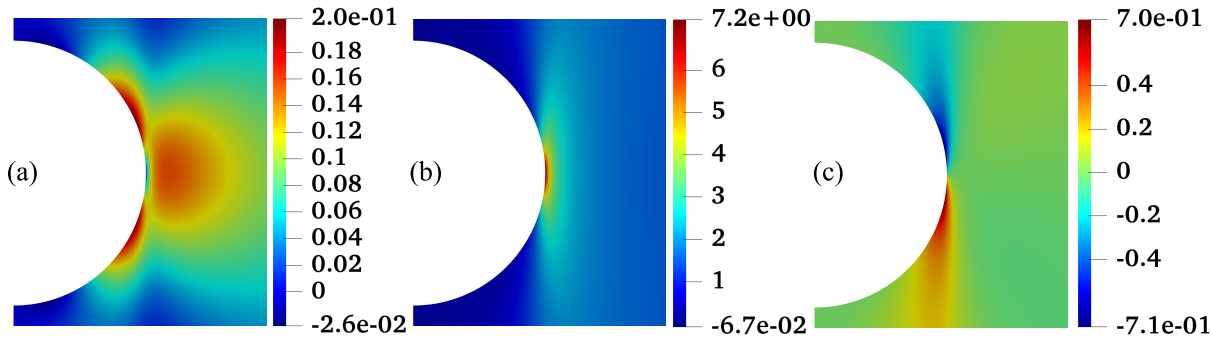

Figure 4.6: Stress fields of composites reinforced by longitudinal straight fibers: (a) Stress in x-direction σ_{xx}, (b) Stress in y-direction σ_{yy}, (c) Shear stress in $x-y$ plane τ_{xy}.

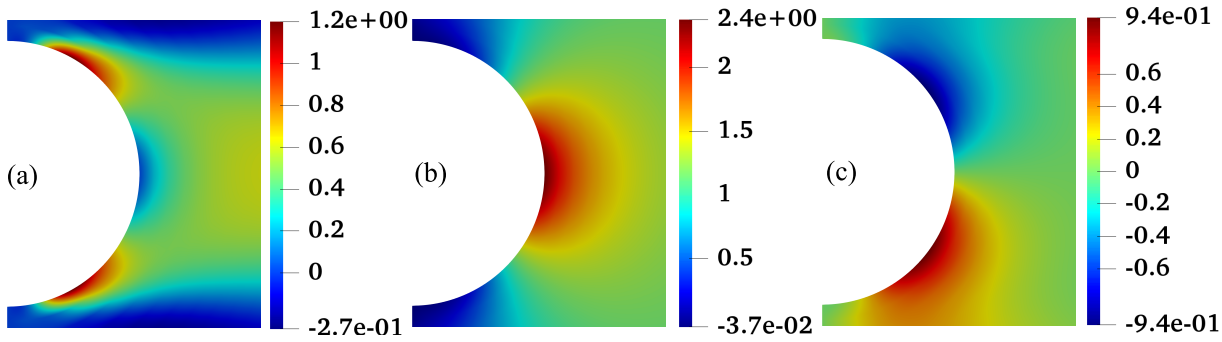

Figure 4.7: Stress fields of composites reinforced by transverse straight fibers: (a) Stress in x-direction σ_{xx}, (b) Stress in y-direction σ_{yy}, (c) Shear stress in $x-y$ plane τ_{xy}.

Table 4.2: Stress concentration factor K_t, stiffness on the top edge E_{yy}, and the Maximum Tsai-Wu failure index vary from different fiber paths: (a) Curvilinear fiber path following semi-circular notch, (b) Concentric fiber path, (c) Longitudinal straight fiber path, (d) Transverse straight fiber path, (e) Isotropic material.

	Fiber path (a)	Fiber path (b)	Fiber path (c)	Fiber path (d)	Fiber path (e)
K_t	3.49	5.02	7.18	2.38	3.08
$\bar{K}$ [GN/mm]	86.72	10.78	88.20	5.11	89.51
Tsai-Wu	0.0261	0.0513	0.0043	0.050	N.A.

4.2 Optimal Fiber Paths

The discussion in the previous section 4.1 is focused on the mechanical properties: Stress concentration factor K_t, the stiffness along the top edge $\bar{K}$, and the maximum Tsai-Wu index Φ in the four different fiber paths. The curvilinear fiber following semi-circular notch reduces the stress concentration around the semi-circular hole the most. On the contrary, the longitudinal fiber path reduces the Tsai-Wu index the most. These indicates that the mechanical properties such as stress concentration factor and Tsai-Wu failure index significantly depend on the fiber orientation. Thus, optimization studies in curviliear fiber paths have been implemented in order to reduces the stress concentration or Tsai-Wu failure index by the use of MATLAB built-in function *fmincon*.

A curvilinear fiber paths has been represented by the 3^{rd} order complete polynomial projecting the surface shape into the two-dimensional contour and implemented multi-objective optimizations using the concept of non-dominated sorting generic algorithm in [16]. Define the curvilinear fiber paths using the same notation introduced in [16], but given that 5-th order complete polynomial function instead of using 3-rd order complete polynomial in order to obtain a high rate of curvature such that

$$\begin{aligned} f(x,y) = C_{00} &+ C_{10}x + C_{01}y + C_{20}x^2 + C_{11}xy + C_{02}y^2 \\ &+ C_{30}x^3 + C_{21}x^2y + C_{12}xy^2 + C_{03}y^3 \\ &+ C_{40}x^4 + C_{31}x^3y + C_{22}x^2y^2 + C_{13}xy^3 + C_{04}y^4 \\ &+ C_{50}x^5 + C_{41}x^4y + C_{32}x^3y^2 + C_{23}x^2y^3 + C_{14}xy^4 + C_{05}y^5 \end{aligned} \tag{4.10}$$

where C_{ij}, where $i, j = 0, 1, 2, 3, 4, 5$ are the coefficients of the 5-th order complete polynomial function. Then, in order to enable to implement optimization in IGA MATLAB framework, the fiber orientation at arbitrary points (x, y) in physical coordinate is needed and derived as

$$\theta(x,y) = \tan^{-1}\left(-\frac{\partial f/\partial x}{\partial f/\partial y} \right). \tag{4.11}$$

4.2.1 Optimization Method

As a optimizer, sequential quadratic programming method has been implemented in MATLAB environment built-in function called *fmincon* to optimize the following two objective functions such that

1.
$$\min_{C_{ij}} K_t, \qquad \text{where } K_t = K_t(C_{ij}) \tag{4.12}$$

2.
$$\min_{C_{ij}} \Phi, \qquad \text{where } \Phi = \Phi(C_{ij}) \tag{4.13}$$

$C_{ij} \in \mathbb{R}$ is refereed to as design variable and the MATLAB built-in function *fmincon* returns the design variables where the objective value satisfies the tolerance of the local minimum.

Problem Statement

In MATLAB environment, the optimization has been implemented using the built-in function *fmincon* with 'sqp' option, which is a sequential quadratic programming method. The problem set-up is same as the one implemented in section 4.1 and the geometry is illustrated in figure 4.1. In addition to this, the another geometry of an optimization study has been implemented with the different radius 40 mm of the semi-circular notched plate (See figure 4.8).

4.2.2 Optimal Fiber Path for Minimum Stress Concentration Factor

Initial condition for the design variables C_{ij} are chosen to be a unit value for minimizing stress concentration factor. The optimal fiber paths generated from MATLAB built-in function *fmincon* are shown in figure 4.9a and 4.9b for the both cases 10 and 40 mm radius of semi-circular notched plates, respectively and the results are summarized as table 4.3. The stress and Tsai-Wu failure index fields are shown in figure 4.10 and figure 4.11.

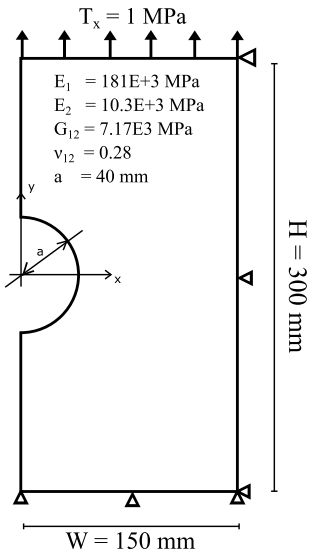

Figure 4.8: Elastic Plate featuring transverse isotropy weakened by a 40 mm semi-circular notch.

Table 4.3: Stress concentration factor K_t, stiffness on the top edge E_{yy}, and the Maximum Tsai-Wu failure index Φ of: (a) optimal fiber path for minimum K_t with radius 10 mm (Opt.1 R10), (b) optimal fiber path for minimum K_t with radius 40 mm (Opt.1 R40), (c) the optimal fiber path for minimum Φ with radius 10 mm (Opt.2 R10), (d) the optimal fiber path for minimum Φ with radius 40 mm (Opt.2 R40).

	Opt.1 K_t R10	Opt.1 K_t R40	Opt.2 Φ R10	Opt.2 Φ R40
K_t	1.25	2.18	7.17	8.88
Φ	0.0198	0.0747	0.0043	0.0080
$\bar{K}$ [GN/mm]	33.37	6.91	88.20	57.83

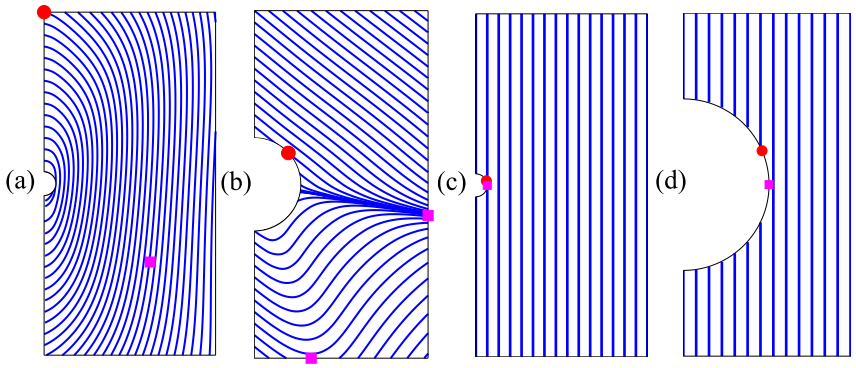

Figure 4.9: Optimal fiber paths for (a) minimum stress concentration factor of radius 10 mm notch, (b) minimum stress concentration factor of radius 40 mm notch, (c) minimum Tsai-Wu failure index of radius 10 mm notch, (d) the magnification of the optimal fiber path (c). Location of stress concentration factors are shown by magenta square, and maximum Tsai-Wu by red circle.

Considering the two results from the implementation of the curvilinear fiber paths following semi-circular notch (figure 4.2a) and concentric fiber paths (figure 4.2b), the curvilinear fibers tend to be having a high rate of curvature around the semi-circular notch in order to reduce the stress concentration factor, and tend to be more straight parallel to the loading condition in order to obtain high stiffness except the semi-circular hole. Based on the curvilinear fiber paths with the radius 10 mm shown in figure 4.9a, the fibers are trying to be more concentric or have more curvature around the semi-circular notch by making the region more compliant than before, and the fibers close to the right-hand edge tend to be more longitudinal straight not to have the stress concentration. Thus, the contour plots of the stress field in y-direction(figure 4.10b) shows the stress concentration around the middle of lower-half of the plate, and the figure 4.9a of the optimal fiber path shows the location of the stress concentration factor precisely, which results from the mechanism explained above.

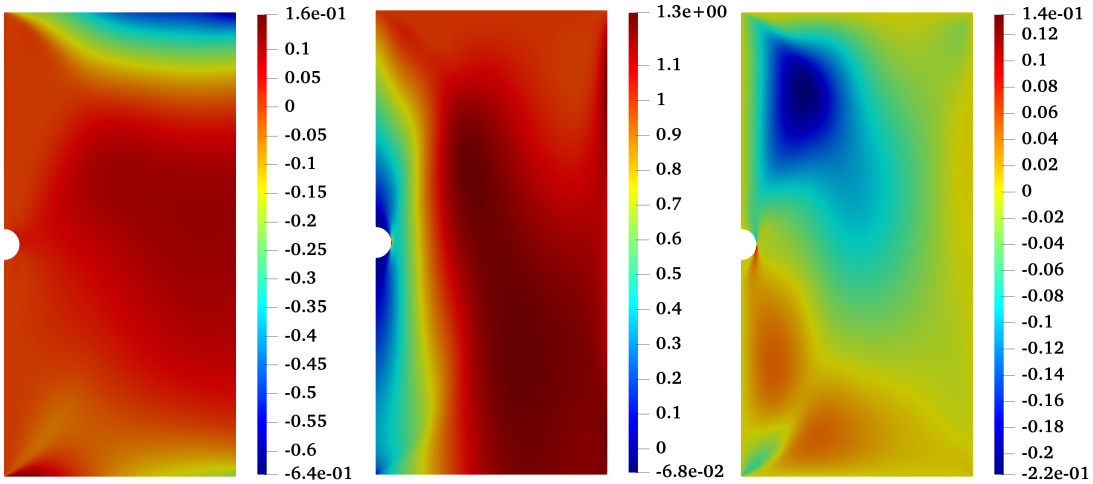

Figure 4.10: Contour plots of optimal fiber reinforced composites of radius 10 mm notched plate for minimum stress concentration. (a) x-component of the stress σ_{xx}, (b) y-component of the stress σ_{yy}, (c) shear component of the stress τ_{xy}.

On the contrary, in the case of radius 40 mm, the curvilinear fibers (4.9b) do not behave like radius 10 mm case because the complete polynomial function that defines the curvilinear fiber paths (4.10) doesn't have enough polynomial order to represent the smoother curve or have high rate of curvature. However, this fiber path seems like that they ended up in trying to follow the semi-circular hole notch due to the low value of completeness order in polynomial. Thus, the optimal case for the radius of 40 mm is not desired one because of low stiffness. The higher order of polynomial is expected to provide the smoother curvilinear fiber path around the semi-circular notch in the future work. The location of stress concentration of this notched plate is not only around the middle point of the right-hand edge (for stress concentration in y-direction), but it is also located on the bottom edge (for stress concentration in x-direction) based on the figure 4.9(b) because both longitudinal (σ_{yy}) and transverse (σ_{xx}) stresses are concentrated on the locations for the same reason discussed on section 4.1.

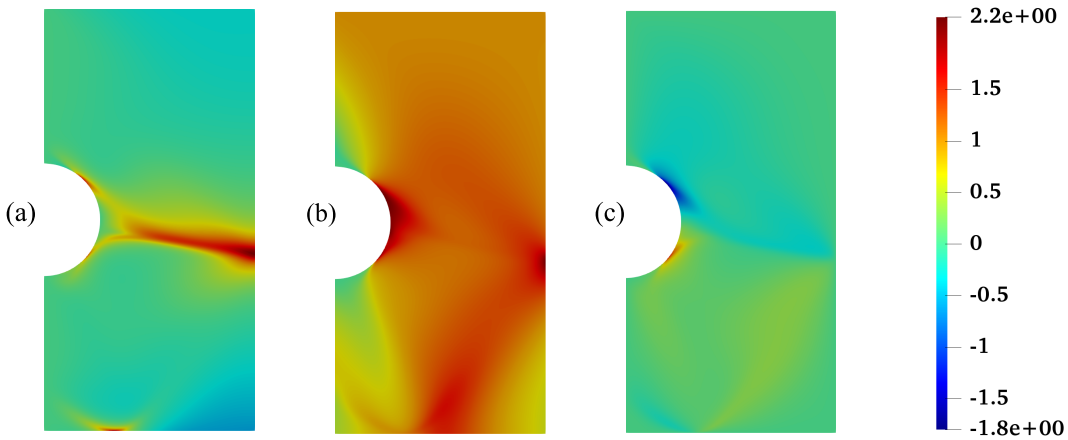

Figure 4.11: Contour plots of optimal fiber reinforced composites of radius 40 mm notched plate for minimum stress concentration. (a) x-component of the stress σ_{xx}, (b) y-component of the stress σ_{yy}, (c) shear component of the stress τ_{xy}.

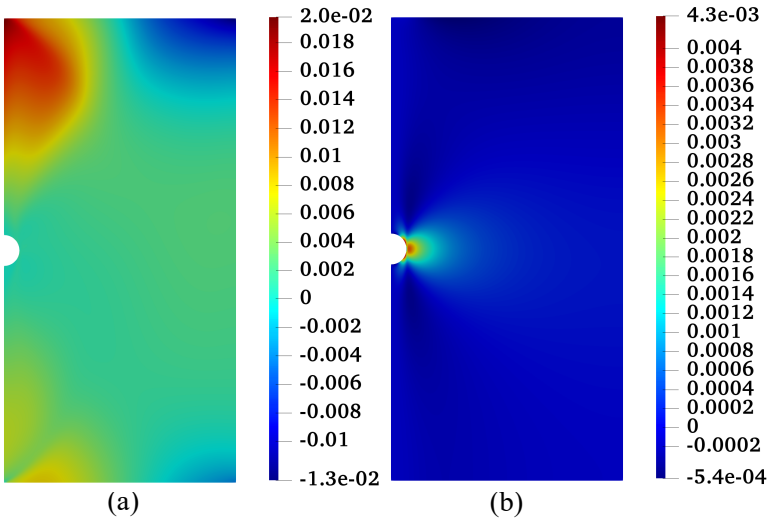

Figure 4.12: Contour plots of the Tsai-Wu failure index of the optimal fiber paths: (a) for the minimum stress concentration factor, and (b) for the minimum Tsai-Wu failure index. of the 10 mm notched plates.

Although the curvilinear fiber paths are represented by the 5^{th} order complete polynomial (4.10), it is not clear that the polynomial has enough capability to represent curvilinear fiber paths. It might be enough to elevate the order of polynomial until the fiber representation becomes smoother, however, it makes the design variables increase more and more and not efficient way to represent the fiber paths. Thus, it may be necessary to find out the another way to represent the fiber paths without restricting the domain of the fiber paths.

4.2.3 Optimal Fiber Path for Minimum Tsai-Wu Failure Index

The optimization study for the minimum Tsai-Wu index has also been implemented under the same condition for the minimum stress concentration. The initial design variables C_{ij} are decided as the longitudinal straight fiber path shown in figure 4.2c such that

$$C_{ij} = \begin{cases} 1 & \text{if } (i,j) = (1,0) \\ 0 & \text{otherwise} \end{cases} \tag{4.14}$$

because this fiber path provide us the minimum Tsai-Wu index based on the four implemented fiber paths (figure 4.2).

As a results of the optimization using the MATLAB, the design variables remained as same as the initial conditions for the both radius 10 and 40 mm cases. The minimum Tsai-Wu failure indices are all same as the ones computed from the longitudinal straight fiber plies (table 4.3).

4.2.4 Damage Initiation Analysis

Based on the table 4.3, the maximum Tsai-Wu index Φ for the fiber path that provides minimum stress concentration for the radius of 10 mm is found as 0.0198 and located at the very top-left node shown in figure 4.9a. This value Φ is slightly less than the one computed from the semi-circular notched plate (Fiber Path (a) of table 4.2) but still about six times higher than the one from the longitudinal straight fiber path, which is optimal fiber path for the minimum Tai-Wu failure index.

Table 4.4 includes the local stresses of the x_1-,x_2-, and shear components, and the com-

Table 4.4: Local stresses and the local stress dominance of ply strengths

	σ_1	σ_2	τ_{12}	σ_1/σ_1^f	σ_2/σ_2^f	τ_{12}/τ_{12}^f
Opt.1 R10	0.0780	0.9417	0.2342	$5.2E-5$	$2.4E-2$	$3.4E-3$
Opt.2 R10	1.112	0.205	0.480	$7.4E-4$	$5.1E-3$	$7.1E-3$

ponents of Tsai-Wu index (figure 4.12a) for the optimal fiber paths shown in figure figure 4.9a of the 10 mm radius semi-circular notched plate. The ratios of local stresses to the ply strengths are calculated as:

For the fiber direction

$$\sigma_1/\sigma_1^f = \begin{cases} \sigma_1/\sigma_{1t}^f & \text{if } \sigma_1 \geq 0 \\ \sigma_1/\sigma_{1c}^f & \text{if } \sigma_1 < 0 \end{cases} \tag{4.15}$$

For the transverse fiber direction

$$\sigma_2/\sigma_2^f = \begin{cases} \sigma_2/\sigma_{2t}^f & \text{if } \sigma_2 \geq 0 \\ \sigma_2/\sigma_{2c}^f & \text{if } \sigma_2 < 0 \end{cases} \tag{4.16}$$

For the shear component

$$\text{The ratio} = \tau_{12}/\tau_{12}^f \tag{4.17}$$

and tabulated in table 4.4.

At the point of the maximum Tsai-Wu failure index, the ratio of local stresses to the ply strengths are found in table 4.4 such that

$$[\sigma_1/\sigma_{1t}^f; \quad \sigma_2/\sigma_{2t}; \quad \tau 12/\tau_{12}^f] = [5.2E-5; \quad 2.4E-2; \quad 3.4E-3].$$

This implies that transverse stress component dominates the matrix strength way more than the others, which may result in matrix failure from the very top-left of the plate and then the crack might grow along the curvilinear fiber path. Thus, even though the object began to experience the failure, it might not immediately be exposed to be an ultimate failure.

On the contrary, the figure 4.12b represents the contour plot of Tsai-Wu failure index for minimum Tsai-Wu of the radius 10 mm notched plate, and figure 4.9c and 4.9d show the location of the maximum Tsai-Wu failure index and the stress concentration factor. The ratios of local stresses to the ply strengths for minimum Tsai-Wu failure indices are calculated in table 4.4 and they are

$$[\sigma_1/\sigma_{1t}^f; \quad \sigma_2/\sigma_{2t}; \quad \tau_{12}/\tau_{12}^f] = [7.4E-4; \quad 5.1E-3; \quad 7.1E-3],$$

which implies splitting crack is the dominance mode in this fiber path since the transverse and shear components of the strengths are dominated by the local stresses the most. Based on the contour plot of the Tsai-Wu index shown in figure 4.12b, the Tsai-Wu index around the semi-circular notch is symmetric against the x-axis, the splitting crack also will occurs from the other location. Moreover, the splitting cracks undergo in the both positive and negative y-direction. Comparing to the optimal fiber path for minimum stress concentration, although the splitting cracks will propagate both positive and negative y-directions in a same time, it is very difficult to predict which fiber configuration will be exposed to be an ultimate failure. Since Tsai-Wu failure criterion only indicates an initial point of failure but the point where ultimate failure will occurs, it is not predictive to conclude which fiber path will dissipate more energy at an ultimate failure. In order to predict the energy dissipation, it is required to incorporate a damage progression analysis and this is one of the future works.

Chapter 5

CONCLUSION

Recently, composites materials are broadly used in a wide range of industries such as aerospace, automotive, renewable energy, and consumer goods. Especially, in aerospace industries, composites materials are applied to large-scale and complex structures in order to take advantage of the lightness and the strength against traditional materials such that steels and metals. Due to the complexity and the large-scale of structures, the manufacturing technology of those structures has been significantly developed, e.g. Automated Fiber Placement(AFP) and Additive Manufacturing(AM). These high manufacturing technology enables to manufacture much more complex and larger-scale structures. For instance, many researchers or engineers are working on the study of manufacturing curvilinear transverse isotorophy(CTI) materials, whose continuous fibers follow curvilinear paths by the use of AM technology.

It is very common to make use of finite element method to conduct a simulation on structures. However, as mentioned in foregoing chapters, the structures are not only getting larger and larger, but also becoming more complex, This inherently provides challenges in mesh generation and refinement in the process of translating a CAD model into a CAE model in order to proceed in structural analysis. Moreover, the geometric representation in the analysis may introduce significant error in the result due to the inaccurate approximation in geometry. Thus, it is necessary to integrate the processes between the modeling part(i.e. CAD model generation) and the analysis(i.e. FEA) to obtain high rate of convergence and greater precision of the solutions, and its integration of CAD model and analysis is called ***Isogeometric Analysis***, which is introduced in Hughes *et al.*, 2005 [17]. In this thesis, NURBS-based Isogeometric Analysis has been implemented, meaning that the NURBS basis

function used in CAD software is also applied to as basis functions in a classical FEM in order to integrate these two processes and to express an exact geometry in an analysis.

To implement NURBS-based Isogeometric Analysis, it is very important to understand the concept of NURBS and these are explained in section 2.2. Discussion on the refinement techniques such as knot insertion and degree elevation are followed subsequently. Then, the element equation can be built using variational method derived in section 2.3. Analysis on composites reinforced by curvilinear fibers are also proposed in section 2.3. Many researchers assume the fiber orientations as constant each element in FEM, however, the fiber orientations are updated each integration point in order to capture the curvilinear fiber paths more precisely in both FEM and IGA. Therefore, the elasticity matrix for transverse isotropy varies inside each element as well.

Implementation framework of NURBS-based Isogeometric Analysis is very similar to the FEA framework. One of the major differences between the two methods is the routine of element equation. As mentioned above, the elasticity matrix can be decided each integration point but element in order to capture the continuous curvilinear fiber paths. The NURBS-based IGA solver enabled by MATLAB environment has already been published online and introduced in [24]. The solver has been modified in order to implement on CTI materials using the concept above. In order to reduce the time-consumption and the inefficiency, parallel computing and vectorization have been implemented.

In order to check the rate of convergence and the mechanical behaviors of CTI materials, the multiple FEM and IGA simulations have been conducted in the following four fiber configurations: (a) curvilinear fiber path following the semi-circular hole notch (figure 4.2a), (b) concentric fiber path following the semi-circular hole notch (figure 4.2b), (c) longitudinal straight fiber path (figure 4.2c), (d) transverse straight fiber path (figure 4.2d) under axial tension on the semi-circular notched plate of plane-stress condition (See figure 4.1). Based on the four error plots (figure 4.3) against mesh size, following conclusions are made:

1. Isogeometric Analysis converges much faster than FEM for all the four different fiber

paths.

2. Isogeometric Analysis meets a transition point where rate of convergence becomes faster in much coarser mesh region than a classical FEM.

Based on the above comments, NURBS-based Isogemeotric analysis shows a good convergence with relatively coarse mesh compared to a conventional FEM, which implies that NURBS-based Isogeometric Analysis is significantly proficient in analysis on large-scale complex structures or CTI materials whose continuous fiber paths are very irregular.

For the mechanical points of views on CTI composites, there exists remarkable facts that are:

1. For the curvilinear fiber path following the semi-circular hole notch, the stress σ_{yy} around the semi-circular notch is significantly less concentrated, and it is about 3.49, which is twice times smaller than the longitudinal straight fiber path.

2. In addition, the stiffness along the top edge is fairly close to the one from longitudinal straight fiber configuration.

3. For the case of concentric fiber path, the stresses σ_{yy} is concentrated at an unusual locations, which is a middle-half of the right-hand edge.

From the fact 1 and fact 2, it is possible to say that: there exists curvilinear fibers close to more transverse direction than the longitudinal direction around the semi-circular notch so that the region may be more compliant than the other regions. This causes a stress concentration reduction around the semi-circular notch. Conversely, the other regions has fibers whose orientations are closer to the longitudinal direction, which makes the region more stiffer and gives the high-level of stiffness on the top edge. The fact 3 has also been happened due to the same mechanism mentioned above. The fiber orientation is getting closer and closer to the longitudinal direction as they are close to the right-hand edge. This

indicates the region around the right-hand edge is more stiffer than the other region so that the stress σ_{yy} is concentrated on the middle point of the right-hand edge. According to the results of our simulations, the mechanical behaviors of the curvilinear fiber reinforced materials depend significantly on the rate of curvatures of the fiber paths, which is fiber orientations.

After the multiple simulations on several curvilinear fibers reinforced composites, optimization study has also been implemented using the MATLAB built-in function *fmincon* with a 'sqp' optipn, which applies a sequential quadratic programming as an optimization method. Optimizations have been implemented in order to reduce (1) the stress concentration factor K_t and (2) the maximum Tsai-Wu failure index Φ for the semi-circular notched plate whose radius is 10 and 40 mm. The optimal fiber paths are shown in (figure 4.8). Polynomial contour map function (4.10) was chosen to provide a design space because this function can express continuous curvilinear fiber paths and does not make the fiber paths crossed each other. Using the optimal fiber path shown in figure 4.9, the stress concentration has been reduced significantly and they are 1.25 and 2.18 for the radius of 10 and 40 mm, respectively. Based on the figure 4.9a (radius 10 mm notched notched plate), the curvilinear fibers are trying to be more compliance around the semi-circular notch, and not having a high rate of the curvature to prevent the stress concentration from the right-hand edge, which directs the stress concentration onto the middle-half of the notched plate. On the contrary, the 40 mm radius notched plate, the curvilinear fibers might tend to follow the semi-circular notch in order to reduce the stress concentration around the notch, but the polynomial function (4.10) that defines the fiber paths does not have enough order of polynomial to represent the smoother curvilinear fiber paths so that the curvilinear fiber paths does not behave like the one from 10 mm radius notched plate. It is necessary to find out the best representation of the curvilinear fiber path in order not to restrict the domain of the fiber paths.

Optimal fiber paths for the minimum Tsai-Wu failure index are also obtained and the fiber paths converged to the longitudinal straight fiber paths (figure 4.9c) for the both radius

of 10 and 40 mm notched plates. When comparing this longitudinal straight fiber path with the radius of 10 mm plate to the optimal fiber path obtained for the minimum stress concentration, the failure of the optimal fiber path for minimum stress concentration factor will occur earlier than the optimal fiber path for minimum Tsai-Wu index, but it is not clear that how the failure progress to an ultimate failure. The optimal fiber path for stress concentration indicates matrix failure and the crack would follow the fiber path. The optimal fiber path for Tsai-Wu failure index will also experience a splitting based on the stress dominance ratio. In the scope of Tsai-Wu failure analysis, the optimal fiber path for minimum Tsai-Wu (longitudinal straight fiber path) is the best. However, it is very difficult to conclude which optimal fiber path will dissipate more energy at the ultimate failure. In order to predict that, it is required to incorporate a damage progression analysis.

In conclusion, NURB-based Isogeometric Analysis shows superior convergence compared to a conventional FEM in the case of complex structures or CTI composites. Mechanical properties of CTI structures are highly dependent on the orientation of the fibers. Consequently, it is crucial to capture the change in curvature in the curvilinear path to accurately model the constitutive behavior. It's shown that the proposed method for evaluating stiffness matrix at each integration point provides much faster convergence rates. As an example case of CTI structures, the curvilinear fiber path following the semi-circular notch had a most compromising mechanical properties with a low stress concentration of 3.49 and high stiffness of 86.72 GN/mm. The curvilinear fibers following the semi-circular notch reduces the stress concentration factor, and the optimal fiber for the minimum stress concentration as well. It is also shown that the longitudinal straight fiber path is the best in terms of Tsai-Wu failure criterion. However, more advanced failure criterion needs to be considered in order to analyze the progression in damage, which can lead to the ultimate failure of the structures.

BIBLIOGRAPHY

[1] *Parallel Computing Toolbox User's Guide*. The MathWorks, Inc., Natick, 2011.

[2] Y. Bazilevs and I. Akkerman. Large eddy simulation of turbulent Taylor-Couette flow using isogeometric analysis and the residual-based variational multiscale method. *Journal of Computational Physics*, 229(9):3402–3414, 2010.

[3] Y. Bazilevs, V. M. Calo, T. J.R. Hughes, and Y. Zhang. Isogeometric fluid-structure interaction: Theory, algorithms, and computations. *Computational Mechanics*, 43(1):3–37, 2008.

[4] J. Austin Cottrell, Thomas J.R. Hughes, and Yuri Bazilevs. *Isogeometric Analysis Toward Integration OF CAD and FEA*. John Wiley and Sons, Ltd., 2009.

[5] M G COX. The Numerical Evaluation of B-Splines. *IMA Journal of Applied Mathematics*, 10(2):134–149, 1972.

[6] Kaven Croft, Larry Lessard, Damiano Pasini, Mehdi Hojjati, Jihua Chen, and Ali Yousefpour. Experimental study of the effect of automated fiber placement induced defects on performance of composite laminates. *Composites Part A: Applied Science and Manufacturing*, 42(5):484–491, 2011.

[7] François Cuvelier, Caroline Japhet, and Gilles Scarella. An efficient way to perform the assembly of finite element matrices in Matlab and Octave. (May), 2013.

[8] Carl de Boor. On calculating with B-splines. *Journal of Approximation Theory*, 6(1):50–62, 1972.

[9] Carl de Boor. *A Practical Guide to Spline*. Springer-Verlag, 1978.

[10] Timothy J. Dodwell, Richard Butler, and Andrew T. Rhead. Optimum Fiber Steering of Composite Plates for Buckling and Manufacturability. *AIAA Journal*, 54(3):1146–1149, 2016.

[11] Wei Gao, Yunbo Zhang, Devarajan Ramanujan, Karthik Ramani, Yong Chen, Christopher B. Williams, Charlie C.L. Wang, Yung C. Shin, Song Zhang, and Pablo D. Zavattieri. The status, challenges, and future of additive manufacturing in engineering. *CAD Computer Aided Design*, 69:65–89, 2015.

[12] Michael Gee, Ekkehard Ramm, and Wolfgang A. Wall. Parallel multilevel solution of nonlinear shell structures. *Computer Methods in Applied Mechanics and Engineering*, 194(21-24 SPEC. ISS.):2513–2533, 2005.

[13] Héctor Gómez, Victor M. Calo, Yuri Bazilevs, and Thomas J.R. Hughes. Isogeometric analysis of the Cahn-Hilliard phase-field model. *Computer Methods in Applied Mechanics and Engineering*, 197(49-50):4333–4352, 2008.

[14] Hector Gomez, Thomas J.R. Hughes, Xesús Nogueira, and Victor M. Calo. Isogeometric analysis of the isothermal Navier-Stokes-Korteweg equations. *Computer Methods in Applied Mechanics and Engineering*, 199(25-28):1828–1840, 2010.

[15] S Honda, K Owatari, and Y Narita. Minimization of stress concentration for laminated composite plates with curvilinearly shaped fibers. *Japan Society of Mechanical Engineers, Part A*, 76(769):1139–1146, 2010.

[16] Shinya Honda, Teruki Igarashi, and Yoshihiro Narita. Multi-objective optimization of curvilinear fiber shapes for laminated composite plates by using NSGA-II. *Composites Part B: Engineering*, 45(1):1071–1078, 2013.

[17] T. J.R. Hughes, J. A. Cottrell, and Y. Bazilevs. Isogeometric analysis: CAD, finite elements, NURBS, exact geometry and mesh refinement. *Computer Methods in Applied Mechanics and Engineering*, 194(39-41):4135–4195, 2005.

[18] Fish Jacob and Belytschko Ted. *A First Course in Finite Elements*. John Wiley & Sons, Ltd., 2007.

[19] Amar Khennane. *Introduction to Finite Element Analysis Using MATLAB and Abaqus*. CRC Press, 2013.

[20] L Peter (Laszlo Peter) Kollar and George S. Springer. *Mechanics of composite structures*. Cambridge University Press, Cambridge ; New York, 2003.

[21] Tod Laursen. *Computational Contact and Impact Mechanics: Fundamentals of Modeling Interfacial Phenomena in Nonlinear Finite Element Analysis*. 2003.

[22] Dirk H.-J.A. Lukaszewicz, Carwyn Ward, and Kevin D. Potter. The engineering aspects of automated prepreg layup: History, present and future. *Composites Part B: Engineering*, 43(3):997–1009, 2012.

[23] S. Morganti, F. Auricchio, D. J. Benson, F. I. Gambarin, S. Hartmann, T. J.R. Hughes, and A. Reali. Patient-specific isogeometric structural analysis of aortic valve closure. *Computer Methods in Applied Mechanics and Engineering*, 284:508–520, 2015.

[24] Vinh Phu Nguyen, Cosmin Anitescu, Stéphane P.A. Bordas, and Timon Rabczuk. Isogeometric analysis: An overview and computer implementation aspects. *Mathematics and Computers in Simulation*, 117:89–116, 2015.

[25] Vinh Phu Nguyen, Pierre Kerfriden, and Stéphane P.A. Bordas. Two- and three-dimensional isogeometric cohesive elements for composite delamination analysis. *Composites Part B: Engineering*, 60:193–212, 2014.

[26] Mahdi Arian Nik, Larry Lessard, and Damiano Pasini. Size-dependent behavior of laminates with curvilinear fibers made by automated fiber placement. *Science and Engineering of Composite Materials*, 22(2):157–163, 2015.

[27] Les Piegl and Wayne Tiller. *The NURBS Book*. Monographs in Visual Communication,. Springer Berlin Heidelberg, Berlin, Heidelberg, second edi edition, 1997.

[28] Marco Salviato and Sean E. Phenisee. Enhancing the electrical and thermal conductivities of polymer composites via curvilinear fibers: An analytical study. *Mathematics and Mechanics of Solids*, (19), 2019.

[29] Gary Mitchel Stanley. *Contiuum-based Shell Elements*. Phd thesis, Stanford University, 1985.

[30] Clemens V. Verhoosel, Michael A. Scott, René De Borst, and Thomas J R Hughes. An isogeometric approach to cohesive zone modeling. *International Journal for Numerical Methods in Engineering*, 87(1-5):336–360, 2011.

[31] Peter Wriggers. *Computational Contact Mechanics*. Willey, 2006.